4-22-2020

INVESTIGATING DORSAL FIN HYDRODYNAMIC FUNCTION OF THE LEMON SHARK, NEGAPRION BREVIROSTRIS

Vivian Lynn Turner
Coastal Carolina University

INVESTIGATING DORSAL FIN HYDRODYNAMIC FUNCTION OF THE LEMON SHARK, *NEGAPRION BREVIROSTRIS*

By

Vivian Lynn Turner

Submitted in Partial Fulfillment of the

Requirements for the Degree of Master of Science in

Coastal Marine and Wetland Studies in the

Department of Coastal and Marine Systems Science

Coastal Carolina University

Spring 2020

Dr. Erin E. Hackett, Major Professor	Dr. Roi Gurka, Major Professor
Dr. Daniel Abel, Committee Member	
Dr. Richard Viso, CMWS Coordinator	Dr. Michael H. Roberts, Dean

Dedication

This thesis is dedicated to my son, Bobby, who continuously inspires me to be the best version of myself. I would not be the person I am today without you.

Acknowledgements

I would like to thank my advisors Dr. Erin Hackett and Dr. Roi Gurka for their unwavering support throughout this process. Their patience, honesty, and knowledge are truly invaluable, and this work would not have been possible without them. To Erin, my journey in this program began with you allowing me to work in the EFL as an undergraduate. Thank you for giving me that initial opportunity as it has been life changing. You are an exceptional role model for all women in science. To Roi, thank you for giving me the opportunity to work with you. Your expertise in fluid mechanics is impeccable, and our conversations have given me the drive and passion to complete this project. Thank you both for encouraging me to keep moving forward despite my failures and making me the scientist I am today; working with you both has been an experience I will never forget. I would like to thank my committee member Dr. Dan Abel for his assistance and for allowing me to participate in his shark biology course during my undergraduate career. Dan, your course turned my childhood fear into an immense fascination and respect for these creatures, and most importantly, inspired the subject for this thesis. I want to thank the Bimini Biological Field Station, the MOTE Marine Laboratory, and the CCU Shark Crew for their assistance obtaining the specimens needed to complete this work. Finally, I would like to thank Coastal Carolina University for providing the funding to conduct this study.

I'd also like to thank my fellow graduate students Matt Stanek, Asif Nafi, Caroline Collatos, and Doug Pastore for teaching me a variety of new skills that I would have never gained without their knowledge, as well as everyone in the Environmental Fluids Lab for all of their assistance with this research (and patience with the unpleasantries associated with working with deceased organisms). I want to thank Tim Hesford for creating the

model used in this thesis. Without his diligence this model would not have been successfully completed so quickly. Finally, I would like to thank my family, Bob, and the Morgan family for their unconditional love and support which allowed me to complete this work.

Abstract

Many sharks are considered highly efficient swimmers. Their swimming efficiency is partially governed by their morphological features such as dorsal fins, which play a role in their hydrodynamics. Most sharks feature two dorsal fins that can vary in size and location over the body. The first dorsal fin has been shown to improve stabilization, maneuverability, and increase thrust production during swimming, whilst the hydrodynamic role of the second dorsal fin is largely unknown. An understanding of the hydrodynamic function of the dorsal fins can be utilized in engineering applications, e.g., to replicate fins on underwater autonomous vehicles to increase energy efficiency during locomotion. To explore the hydrodynamics of the second dorsal fin and seek solutions applicable to the biomimetic world, we selected a species with a second dorsal fin that is almost as large as its first dorsal fin: the Lemon Shark. An enlarged second dorsal fin is an uncommon characteristic among sharks. Here, we performed a comparative study between the Lemon Shark and another shark species that has a small 2nd dorsal fin compared to the first: the Spinner Shark. We experimentally investigated the hydrodynamic role of the 2nd dorsal fin of the Lemon Shark and used particle image velocimetry to measure the fluid dynamics in its wake. Measurements were collected in the streamwise-spanwise plane behind the 1st and 2nd dorsal fins, as well as the caudal fin for deceased sharks of both species (Spinner Shark and Lemon Shark). In addition, a 3D flexible Lemon Shark model was also used to compare with the deceased specimens. Using the measured data, we: i) evaluated the characteristics of the specimens' and model's wake and ii) examined what effect these characteristics have on the hydrodynamic forces acting on the sharks. The presence of a vortex street in the wake was identified using proper orthogonal decomposition (POD). Based on the POD, the vortex street characteristics such as:

wavelength, cross-stream distance, spacing ratio, Kronauer stability, von-Karman stability, and Strouhal number were computed. These wake characteristics were used to compute the thrust, and the drag was computed based on the momentum deficit in the wake. Results showed a stable vortex street developed in the wake behind the 1st dorsal fin for both species. Although the Lemon Shark had two dorsal fins similar in size, the Lemon Shark's 2nd dorsal fin did not feature a vortex street in the wake. The size of the wake was larger than that of the 1st dorsal fin, which resulted in higher drag behind the second dorsal fin compared to the first dorsal fin. It was also found that the flow behind the 2nd dorsal fin did not fully recover prior to reaching the caudal fin, which indicated some interaction with the wake formation behind the caudal fin. It appeared that this interaction reduced the size of the overall wake for the Lemon Shark. Ultimately, this smaller wake resulted in lower drag behind the caudal fin compared to a species with only one large dorsal fin, like the Spinner Shark.

Table of Contents

List of Tables

List of Figures

List of Symbols and Acronyms

$\boldsymbol{A}$: Eigenvector matrix of vorticity in normal direction

A: Wetted area

AUV: Autonomous underwater vehicle

a: Vortex wavelength

a_n: Coefficients correspondent to the eigenfunctions of the vorticity in normal direction

b: Vortex cross stream distance

CFD: Computational fluid dynamics

C_D: Drag coefficient

C_T: Thrust coefficient

D: Drag per unit length

FOV: Field of view

FSI: Fluid-structure interaction

f: Vortex shedding frequency

fps: Frames per second

h_f: Height of the dorsal/caudal fin

h: Width of the wake in the spanwise direction

L: Characteristic length

LS-C: Experiment name for measurement of Lemon Shark wake behind the caudal fin

LS-1DF: Experiment name for measurement of Lemon Shark wake behind the first dorsal fin

LS-2DF: Experiment name for measurement of Lemon Shark wake behind the second dorsal fin

LMS-C: Experiment name for measurement of Lemon Shark model wake behind the caudal fin

LMS-1DF: Experiment name for measurement of Lemon Shark model wake behind the first dorsal fin

LMS-2DF: Experiment name for measurement of Lemon Shark model wake behind the second dorsal fin

L_T: Total body length of shark

l_{th}: Maximum diameter of the body

M: Number of data points within a single PIV frame

N: Number of PIV snapshots or frames collected

PCL: Pre-caudal length

PIV: Particle image velocimetry

POD: Proper orthogonal decomposition

Q: Symmetric martix of vorticity in the normal direction

q: Total number of eigenfunctions

r: Physical unit to pixel conversion factor

Re: Reynolds number

SNR: Signal-to-noise ratio

SS-C: Experiment name for measurement of Spinner Shark wake behind the caudal fin

SS-1DF: Experiment name for measurement of Spinner Shark wake behind the first dorsal fin

St: Strouhal number

TBF: Tail-beat frequency

x_*: Pixel displacement in ether spanwise or streamwise direction

x: Streamwise direction

u: Velocity in the streamwise direction

$\bar{u}$: Mean streamwise velocity

U_s: Speed of the vortex system

U_w: Wave speed of the vortices

U_∞: Freestream velocity

V: Velocity in spanwise or streamwise direction

w: Velocity in the spanwise direction

z: Spanwise direction

1DF: First dorsal fin configuration

2DF: Second dorsal fin configuration

Δt: Time between PIV image pairs

ν: Kinematic viscosity

λ: Eigenvalues of vorticity in the normal direction

ρ: Density of water

ϕ_n: Eigenfunctions of the vorticity in the normal direction

$\widehat{\omega}_y$: Vorticity in the normal direction

1.0 Introduction

The fluid dynamics of the ocean are complex and constantly changing due to variations in currents, waves, turbulence, salinity, temperature, etc. These constantly evolving conditions create a challenging environment in which fish must adapt to for survival. Although fish can adapt to these complex oceanic conditions, the operation of underwater man-made vehicles can be hindered. To improve operation of these vehicles, scientists look to the field of *biomimicry* for a sustainable solution. Biomimicry creates technological advancements using the inspiration of the natural world, one example of this includes fish swimming. Due to various swimming styles (i.e. carangiform, thunniform) and body shapes (slender or bluff bodies) that promote adaptation to changing oceanic conditions, fish swimming is a highly beneficial area of study (Kozlov et al., 2015; Fish et al., 2003). More specifically, how certain morphological features influence the swimming capabilities of fast swimming and/or migratory fish.

Cartilaginous fish, like sharks, have evolved specific morphological adaptations for swimming in the variety of habitats, such as the open ocean or mangrove systems. These morphological adaptations include the caudal fin, which is considered as the primary mechanism of locomotion for sharks. Another common morphological feature is median fins like the anal fin and dorsal fins, which vary in both presence and size depending on species. Most species possess two dorsal fins, and commonly the second dorsal fin is smaller in size compared to the first. However, there are few species that possess a second dorsal fin almost equal in size to the first dorsal fin.

Experimental studies have some evidence of dorsal fin contribution to efficient locomotion in sharks (Thomson and Simanek, 1977; Webb and Keyes, 1982; Wilga and Lauder 2000; Fletcher et al., 2014; Mia et al., 2017), yet some questions remain unanswered. One such question is the hydrodynamic function of the second dorsal fin. To better define the hydrodynamic functionality of this second dorsal fin, we focused on the Lemon Shark (*Negaprion brevirostris*). The Lemon Shark features a second dorsal fin similar in size to the first dorsal fin, an uncommon feature among sharks. Although the Lemon Shark's physiology and behavior have been extensively studied, the functionality of this second dorsal fin both physically and biologically is not well understood. To examine possible hydrodynamic functions of the second dorsal fin of sharks this thesis studies the fluid-structure interaction using an interdisciplinary approach that combines knowledge from the fields of biology, oceanography, and engineering.

We study the fluid-structure interaction experimentally using deceased shark specimens and a model which are placed individually into a large recirculating flume filled with water. The water's speed set to flow across a shark is assumed to be equivalent to a shark's cruising speed and results in a wake behind the organism. This wake is measured behind the dorsal fins and caudal fin using a non-intrusive flow imaging technique. From these measurements we can gain insight into the fluid-structure interaction of sharks and thus possible hydrodynamic functions. The following thesis presents background on general aquatic animal propulsion with a focus on shark propulsion in Section 2, followed by the objectives of the study in Section 3. Experiments conducted and methods applied for the analysis of this data are presented in Section 4, and Section 5 examines and compares

results from the experiments and analysis conducted, along with a summary and conclusion of this study in Section 6.

2.0 Background

To examine dorsal fin function in sharks, this study focuses on the fluid-structure interaction between a shark and the fluid its submerged within. Fluid-structure interaction (FSI) is the coupling between a structure and the surrounding fluid. FSI is characterized by stable or oscillatory interactions of multiple continuum fields, where the forces of the fluid and the structure are transferred across boundaries. If the structure deforms, then both the fluid velocity and the continuum field will change (Marius and Carmen-Anca, 2012). This interaction also leads to stresses exerted on the structure, which can result in deformations (strains) depending on the pressure and the velocity of the flow as well as the material properties of the structure.

The most common example of FSI is water flow over a cylinder. As water flows towards the cylinder, viscosity slows the movement of fluid parcels close to the surface of the cylinder. The decrease in movement of fluid parcels creates a region where shear forces are dominant. This shearing leads to the development of a thin moving fluid layer, otherwise known as a boundary layer around the surface of the cylinder. If these fluid parcels decelerate or reverse direction due to an adverse pressure gradient, then the neighboring fluid parcels will begin to move away from the surface, causing a boundary layer separation. Therefore, the boundary layer characteristics are dependent on the external pressure gradient around the object.

For most FSI cases, pressure increases over the rear half of the object, and flow separation occurs when the momentum at the surface of the body can no longer overcome this adverse pressure gradient (Bushnell and Moore, 1991). Due to this pressure gradient the body can experience two types of drag force: frictional and pressure (or form) drag (Anderson, 2011). If the body is dominated by frictional drag then it is considered streamlined, and if the body is dominated by pressure drag then it is bluff or blunt, as illustrated in Figure 1 (Anderson, 1989; 2011). The frictional drag over the body is created by the large shear developed within the boundary layer and expands across the entire object surface. These boundary layers separate from the body in the downstream direction behind it and form a wake (Figure 1). The wake is a function of the interaction between the flow dynamics in the boundary layer and the morphologic features of the body. The wake is commonly characterized by a momentum deficit formed by the merging of the boundary layers from the top and bottom surfaces of the object at the trailing edge region (of the object), resulting in a series of vortices that may form (under specific flow conditions) an organized pattern, known as a "vortex street", shown in Figure 2 (von-Karman, 1934). A vortex street is a series of alternating positive and negative vortices in a fixed position that are shed from the body (von-Karman, 1934; Anderson, 2011). For streamlined bodies, like tunas or sharks, the momentum deficit is smaller, and the vortices created are relatively more uniform/organized compared to a bluff body.

From the wake and vortex street (if present) the characteristics and forces acting on the body can be estimated. The hydrodynamic forces exerted on the body can be estimated from the wake by Newton's 3rd law. The drag is directly related to the wake momentum deficit (Goett, 1939), which is proportional to the streamwise velocity deficit developed in

the wake. If the body is not accelerating, or in steady conditions, thrust is the inverse of drag and the two forces are typically in equilibrium.

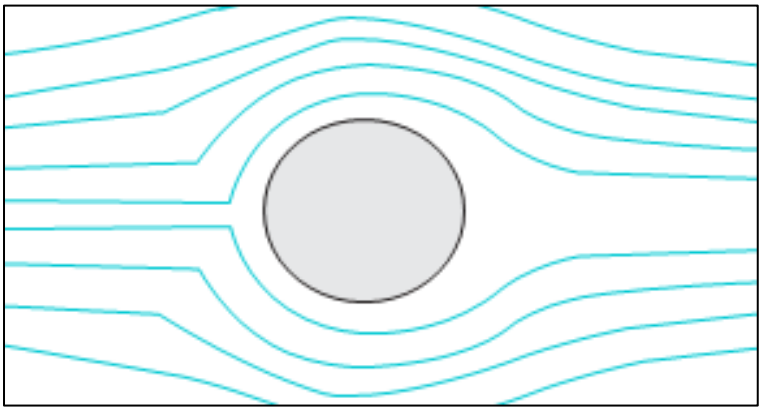

Figure 1: Flow around a cylinder depicted as streamlines. The boundary layer separates at the anterior portion of the cylinder and a wake is created. The size of the wake is dependent on the flow dynamics and the geometry of the object.

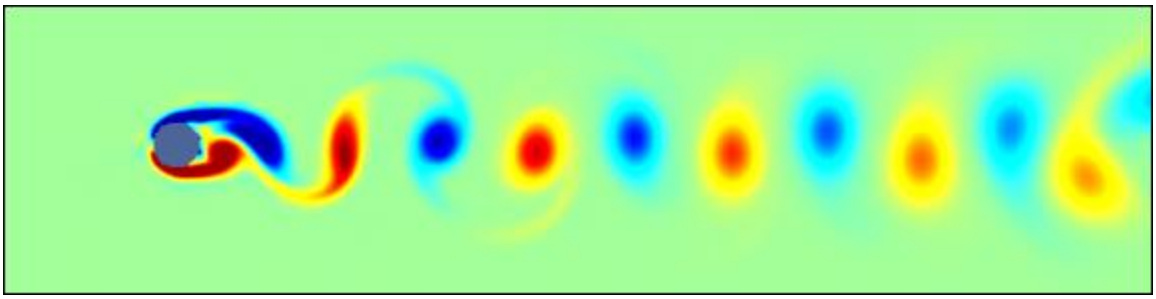

Figure 2: Vortex street behind a cylinder. The flow moves from left to right and the color indicates vorticity (red equating to a positive vortex and blue a negative vortex). Alternating positive and negative vortices are shed from the cylinder into the flow (Intensity of vortices is irrelevant). Forces such as lift and thrust can be estimated from a vortex street (image provided courtesy of Krishnamoorthy Krishnan).

2.1 Propulsion of Aquatic Animals

Fast-swimming fish like tuna and swordfish have a streamlined body. These organisms swim by undulation in combination with the oscillation of fins. This swimming method generates an acceleration or thrusting force for various biological functions like catching prey or escaping predators (Daniel, 1984). These fish can also reduce flow-separation and overall drag, presumably through turbulence modulation (Bushnell and Moore, 1991).

The overall motion of the body plays a large role in the hydrodynamics of aquatic animal propulsion. This overall motion is defined by four general modes of propulsion for fish: anguilliform, carangiform, subcarangiform, and thunniform, as shown in Figure 3 (Gray, 1953; Lighthill, 1970; Webb, 1975, 1978; Lauder and Tytell, 2006). These modes of undulation correspond to the lateral motion of the body (i.e. whole body or posterior end of the body), and are common mechanisms for aquatic propulsion in most pelagic fish (Bone, 1978; Hertel, 1966; Lighthill, 1970; Lindsey, 1978; Webb, 1975, 1978; Webb and Weihs, 1983; Lauder and Tytell, 2006). Undulation results in a wake generated behind the fish, which can contain a vortex street. For some pelagic fish, like bony fish (i.e. Giant Danio and Bream), combining undulation with a series of continuous dorsal and ventral fins along the body produces a vertical trailing edge at each fin along the body (Lighthill, 1970). This body motion and trailing edge provides a more immediate exchange of momentum, which can reduce the size of the overall wake (Gray, 1953; Lighthill, 1970). Therefore, the mode of undulation a fish produces can influence the overall swimming speed.

The mode of undulation can also affect the swimming efficiency of a fish. Swimming efficiency is defined as the ratio of work performed to the expended energy as measured

over time (Maertens et al., 2015). To achieve maximum efficiency (which is needed for migration), a swimmer must obtain the highest swimming speed using the least amount of energy. Carangiform swimmers specifically, have been thought of as efficient swimmers due to prevention of momentum exchange produced by the dorsal fins (Figure 4). Momentum exchange refers to the product of mass and velocity produced and transferred by features of the body. The momentum developed from the dorsal fins is no longer reabsorbed back into the body and mixed into the boundary layer, thus improving the body's swimming efficiency (Lighthill, 1970). The prevention of this momentum exchange is the result of where the undulation occurs on the body. For carangiform swimmers the amplitude of undulation is only significant in the posterior half of the fish (Lighthill, 1970; Webb, 1975; Lauder and Tytell, 2006).

To maximize efficiency, carangiform swimmers depend on the side forces produced by lateral movement of undulation (Lighthill, 1969; 1970). These side forces can result in additional body movements (i.e., yaw) that can be considered as a "recoil" process (Lighthill, 1969). If the recoil is large, then efficiency becomes low as energy of the fish would be expended on counteracting the recoil. Swimming efficiency can also be dependent on morphology of the body. Carangiform swimmers have developed physical features such as narrow necking, or a reduction of depth in the cross section of a fish, to presumably reduce the recoil created by the undulation. Therefore, the anterior portion of the body prior to the caudal fin plays an important role in drag reduction without a loss in thrust for a swimming fish (Lighthill, 1970). Despite Lighthill's (1970) emphasis on the importance of the anterior portion of the body, he argued that dorsal and ventral fins do not contribute to vortex development in the wake region. Lighthill (1970) hypothesized that

because the role of these fins does not significantly contribute to carangiform undulation (due to prevention of momentum exchange), then they cannot contribute to the overall forces acting on carangiform fish.

Later research has shown Lighthill's hypothesis may not be true, and that median fins in carangiform fish, shown in Figure 4, can produce individual vortices in their wake, which interact constructively or destructively to affect the hydrodynamic forces acting on the body (Drucker and Lauder, 2001; Wolfgang et al., 1999). The Giant Danio sheds vortices from the dorsal and anal fin, which affect the flow dynamics near the caudal fin when turning (Wolfgang et al., 1999). A numerical model for straight-line swimming of the same fish shows energy recapture from vortices shed upstream interacting with the caudal fin, which leads to a generation of thrust (Wolfgang et al., 1999). Drucker and Lauder (2001) found that the oscillating soft dorsal fin of a bluegill sunfish can contribute to the wake depending on swimming speed. At slow swimming speeds, the median fins are determined to be hydrodynamically inactive, meaning they have no contribution to the hydrodynamic forces acting on the fish. However, at higher swimming speeds a vortex street behind the dorsal fin can be seen. This street is the result of vortices shed at the trailing edge of the dorsal fin that combine constructively with the wake behind the body of the fish to enhance thrust (Drucker and Lauder, 2001; Tytell, 2006). For knifefish, a reverse vortex street is shed behind the anal fin and is the primary thrust producer for the knifefish, making it a highly efficient swimmer (Taylor et al., 2013).

Overall, the geometry of the fish plays a role in its hydrodynamics to prevent flow separation, which leads to reduction in drag and promotion of thrust (Bushnell and Moore, 1991; Lauder and Tytell, 2006). However, the dominant source of drag experienced

depends on the flow conditions, how close the body is to the air-water interface, and the relative contributions of inertial, gravitational, and viscous forces within the flow (Fish, 1998). Drag can be reduced through the utilization of appendages or other anatomical features, various behaviors, and secretion of materials, such as mucus (Fish, 1998). Therefore, it is important to understand how the biology of the fish relates to its swimming.

Bony fish have a body shape that directly relates to its swimming kinematics (Webb and Keyes, 1982). The more fusiform the shape, the less flexible the body is and the narrower the peduncle region is before the caudal fin (Figure 4), resulting in a fast swimming fish. Blue gill sunfish produce a vortex ring, or alternatively fluid that forms a closed loop in the wake of the tail (Anderson, 2011), like that of birds in air (Drucker and Lauder, 1999). Drucker and Lauder (1999) calculated spanwise vorticity generated from the pectoral fins and compared these results to vortices in the wake. They found the spanwise vorticity shed from the pectoral fins reflects a transfer of momentum in the wake that relates to lift and drag forces created by the fish (Drucker and Lauder, 1999). For a swimming bluegill sunfish, vortices are generated at swimming speeds between 0.5 and 1.0Ls^{-1} (Ls^{-1}= body lengths per second) (Drucker and Lauder, 1999). Once the swimming speed increases to 1.0-1.5Ls^{-1}, the mean lift on the fish is doubled from ~6.59N to ~12N due to production of a linked vortex ring pair from the pectoral fins, as shown in Figure 5.b, that transition into the wake and alter the orientation of flow in the wake (Drucker and Lauder, 1999). Recent research on bony fish has suggested that vortices generated by the body (without the presence of dorsal/ventral fins) are not strong enough to advect downstream and contribute to the overall wake dynamics, and the presence of a sharp trailing edge (such as a median fin) is needed to create a flow that has potential to interact with the wake behind the body

(Brooks and Green, 2019; Lui et al., 2017). Fusiform shaped bony fish and cartilaginous fish have similar swimming kinematic properties; however, the median fins of cartilaginous fish, like sharks, have larger gaps between them, which may promote an increase in swimming efficiency (Webb and Keyes, 1982; Lighthill, 1970).

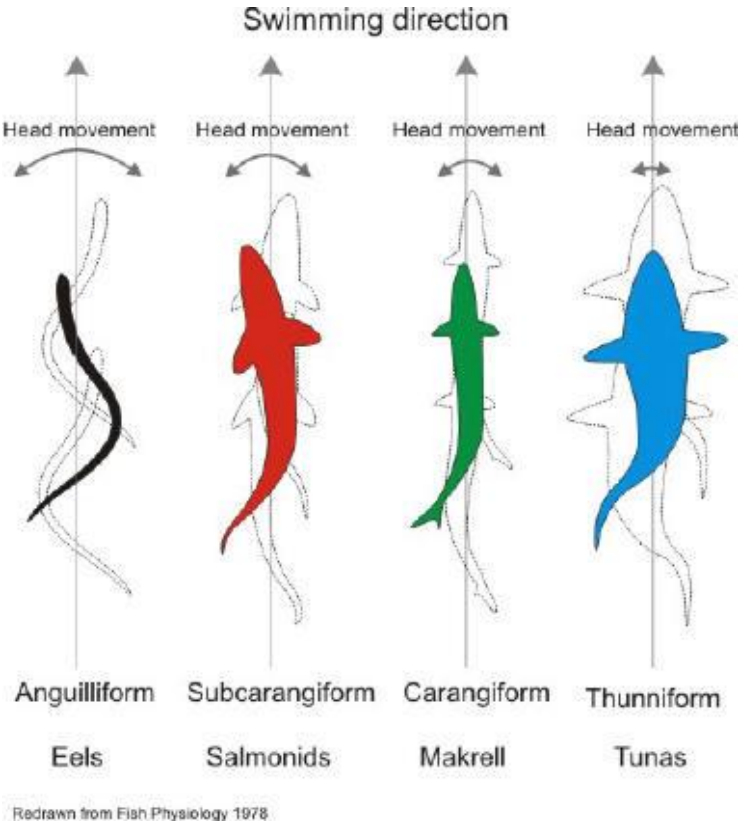

Figure 3: Modes of undulation from left to right: anguilliform, subcarangiform, carangiform, thunniform (reproduced here from Rossi et al., 2011).

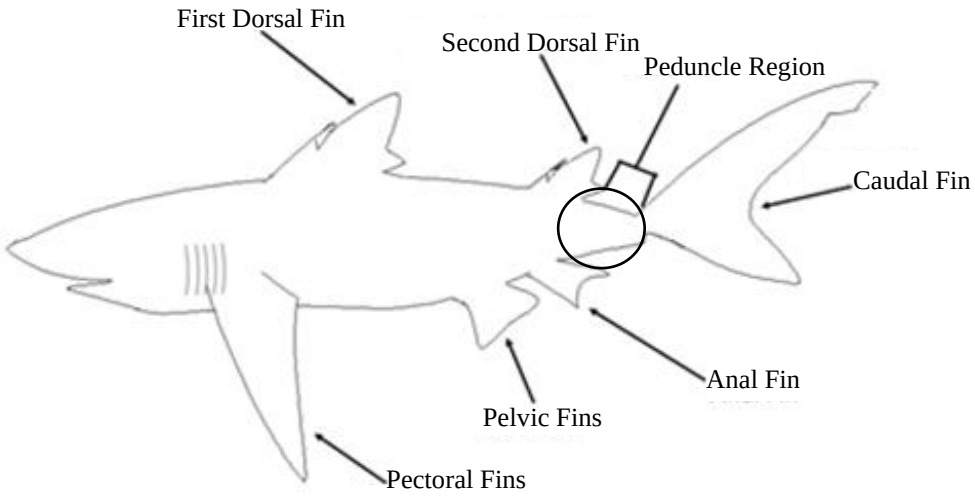

Figure 4: Appendages of a shark. The median fins of a shark consist of the first and second dorsal fins, and anal fin.

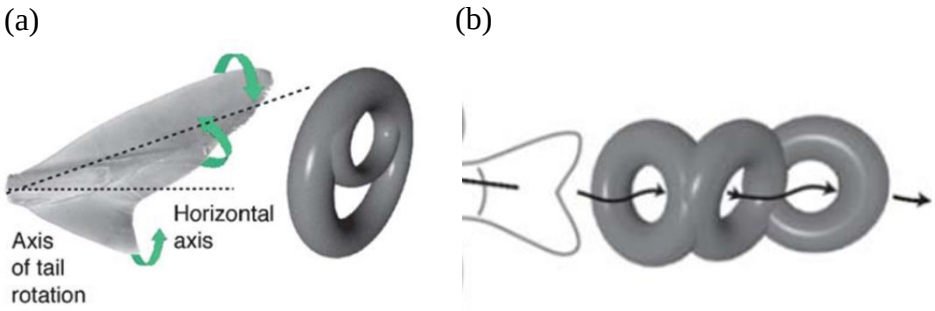

Figure 5: Vortex ring comparison of a spiny dogfish (a) and a bluegill sunfish (b) during steady swimming (reproduced here from Fish and Lauder, 2006).

2.2 Shark Propulsion

Unlike bony fish that have a swim bladder to maintain lift, most sharks must self-generate lift due to their negative buoyancy (Moss, 1984; Phileger, 1998; Wilga and Lauder, 2002). The notable exception to this negative buoyancy is larger, slower moving sharks like the whale shark and basking shark, which are almost neutrally buoyant due to high levels of fat in their body tissue (Moss, 1984). Some sharks also have low metabolic rates compared to most fish due to ram ventilation, a respiratory process that allows water to be forced through the gills (Graham et al., 1990). Ram ventilation allows sharks to swim continuously at cruising speeds without increasing metabolic costs and increasing swimming efficiency (Graham et al., 1990). Swimming efficiency and force generation of sharks are dependent on the mode of undulation, which can be subcarangiform, carangiform, or thunniform depending on species (Webb and Keyes, 1982; Shadwick and Gemballa, et al., 2006). In combination with the mode of undulation, manipulation of the flow can occur through the various morphological features of the sharks such as oscillation of the caudal fin, lift generation by the pectoral fins, the structure of dermal denticles across the skin, shape of the dorsal fins, and even the shape of the head (Figure 4). In this section, we will discuss how various appendages have resulted in different manipulations of the flow, with emphasis on the caudal fin and dorsal fins.

The caudal fin, or tail, acts to counteract negative buoyancy (Fletcher et al., 2014) and contribute to propulsion through lateral oscillation, which generates both thrust and lift (Lighthill, 1975). Most sharks have a caudal fin that can be described as a heterocercal tail; an asymmetrical tail with an upturned notochordal axis. The tail consists of an upper lobe

known as the epichordal lobe, and a lower lobe known as the hypochordal lobe (Thomson and Simanek, 1977; Moss, 1984). As the tail oscillates, the epichordal lobe rotates so that the rear edge of the lobe creates a leading-edge or moves to a leading position in the later part of a transverse tail beat (Thomson and Simanek, 1977; Moss, 1984). Thomson and Simanek (1977) suggested that because of the heterocercal shape of the tail there is a possibility of instability (pitching of the front end of the body) while swimming, which could potentially aid or hinder a shark. Overall, Thomson and Simanek (1977) hypothesized that the function of the caudal fin is to create a force that acts on the center of mass of the shark. This force has two components: the along-body and transverse force. During each lateral beat of the tail the along-body force is composed of a thrust that is directed horizontally depending on the angle of the heterocercal tail (Thomson, 1976; Thomson and Simanek, 1977). The transverse force is a thrust directed upward that results from the rotation of the tail about the vertical spanwise plane. These two thrust components (transverse and along-body) create a combined thrusting force used to propel a shark forward through the water.

Wilga and Lauder (2002) investigated caudal fin mechanics experimentally using Leopard Sharks and found that despite changes in pitch, the caudal fin maintains a consistent angular relationship with the rest of the body. In contrast to bony fish that form a jet surrounded by one vortex ring (the radius of an area of full circulation) in the wake, the oscillation of the tail creates a jet surrounded by a dual vortex ring, which was identified visually using PIV measurements (Wilga and Lauder, 2002). This dual vortex ring, shown in Figure 5.a, is formed as a result of one vortex ring shed after every tail beat, and the second ring attaches with the first after it is produced by the subsequent tail beat, thus forming a smaller ring

inside a larger ring (Wilga and Lauder, 2002). However, this conjecture is not well supported by the data presented in the study. Wilga and Lauder (2002) assumed that the orientation of the dual vortex ring provided evidence that the function of the tail provides torque around the center of mass of the shark, and concluded differences in the shape of the tail between two species did not seem to have an effect on the function of the tail. Wilga and Lauder (2002) also stated that the angle of the vortex ring may not be solely related to the angle of the tail, but the movement of dorsal, ventral, and pectoral fins could also play a role.

Lighthill (1970) initially stated there is no interaction between median fins and the caudal fin for carangiform swimmers however, he later proposed the idea that sharks have different swimming kinematics, such as fast swimming, as a method to promote flow interactions between median fins (Figures 3 and 4). Webb and Keyes (1982) tested this theory with several species of sharks using video recording observations in a tank to determine kinematic parameters such as tail-beat frequency (TBF), which is the number of tail beats per second or the oscillation rate of the caudal fin, specific amplitude (the average displacement of the tail over two or more tail beats) and specific wavelength of the propulsive wave, which is the average wavelength of the wave resulting from undulation (Webb and Keyes, 1982). Unlike bony fish where thrust is only affected by tail-beat frequency (Webb and Keyes, 1982), it was found that TBF, wavelength and amplitude of the propulsive wave affect the thrust of sharks (Webb and Keyes, 1982). Webb and Keyes (1982) concluded that this difference could be related to the interactions of the flow between the dorsal and caudal fins.

It is commonly accepted that dorsal fins serve as stabilizers to prevent roll and allow for quick turning (Fletcher et al., 2014). The position of insertion of the first and second dorsal fin are highly consistent for most species of sharks; however, the second dorsal fin is not present in all species of sharks (Thomson and Simanek, 1977). The size and growth of the two dorsal fins differ greatly between species, and the smaller the fin size the faster the growth rate of the fin (Thomson and Simanek, 1977). Thomson and Simanek (1977) also suggest an intricate role for each fin type (dorsal, pectoral, etc.), but suggest no variation in function across species. However, more recent studies (Lingham-Soliar, 2005; Mia et al., 2017; Payne et al., 2016) have shown that Thomson and Simanek's (1977) idea that the role of each fin does not change between species may not be valid.

One of the more controversial examples is a study by Payne et al. (2016), which found from measuring body posture that some species can use the first dorsal fin to reduce the cost of transport. Great Hammerhead Sharks have been observed to swim at an absolute roll between 50° and 75°, due to an elongated dorsal fin. Using an accelerometer to estimate pitch and roll angles, it was found that the Great Hammerhead swam between these angles while ascending, descending, and swimming at a constant depth (Payne et al., 2016). Swimming at an angle generates lift through the dorsal fin and reduces drag over 10% while using about 8% less energy to swim (Payne et al., 2016). It is important to note that natural behavior can be difficult or impossible to observe directly (Brewster et al., 2018), and this behavior has only been observed without the presence of an accelerometer on the peduncle within the past couple of years, which can be seen in Figure 6.

Other studies have shown the first dorsal fin for the White Shark and Tiger Shark functions as a stabilizer due to a series of collagenous fibers that are found on the body and extend

into the fin (Lingham-Soliar, 2005). These fibers lie at a large angle on the body, and during fast swimming the fibers contract from an internal hydrostatic pressure to stiffen the dorsal fin (Lingham-Soliar, 2005). Another study by Mia et al. (2017) suggested that the placement of dorsal fins on the body could indicate dorsal fin function. When comparing the Spiny Dogfish and Bamboo Shark, it was found that the first and second dorsal fin of the Bamboo Shark contributed to overall thrust production; whereas the Spiny Dogfish produced a net drag in the wake of the first dorsal and acceleration in the wake of the second dorsal fin (Mia et al., 2017). Little is known about the second dorsal fin, but it is hypothesized that the second dorsal fin has little effect on the flow between the first dorsal fin and the caudal fin at least at cruising speeds (Lighthill, 1970). The hypothesis proposed by Lighthill is based on evidence that most pelagic species of sharks having a second dorsal fin that is small compared to the first dorsal fin, and the tapering shape of the posterior end of the body prevents the second dorsal fin from contributing to vortex shedding in the flow (Webb and Keyes, 1982).

These studies mentioned above have shown various aspects of sharks and their influence on propulsion including the streamline shape of their body, the oscillation of their caudal fin, and the size and internal structure of the dorsal fin. There is still a need for further study of fin function in sharks as most of the studies presented provide more questions than answers (Irschick et al., 2017). Some sharks have a smaller or nonexistent second dorsal fin; however, several species have a second dorsal fin that is almost as large as its first dorsal fin. Figure 7 shows a Lemon Shark, a species of shark that has this feature of two large dorsal fins. Unlike fellow species with two large dorsal fins that swim slowly, the Lemon Shark is considered a fast moving, long distance migratory shark.

Figure 6: Great Hammerhead shark swimming on its side (photo courtesy of Jacinta Shackleton).

Figure 7: Juvenile Lemon Shark (photo courtesy of Mark Corcoran).

2.3 Lemon Shark

The Lemon Shark (*Negaprion brevirostris*) is found along the Atlantic East coast from Brazil to New Jersey, with the predominant population located off the coast of Florida and the Bahamas (Wetherbee et al., 1990). Size of juveniles at birth averages around 39cm pre-caudal length (PCL) and male adults reach a PCL of about 175cm, whereas females are slightly longer with a PCL of 185cm (Brown and Gruber, 1988). Juveniles live in mangrove systems, which provide a shallow nursery ground for juveniles as means of protection from larger predators (Guttridge et al., 2012). As juveniles reach sexual maturity, they become highly migratory, expanding their home range to tens of thousands of square kilometers (Sundström et al., 2001). Overall, Lemon Sharks are relatively fast swimmers compared to other species of sharks but differ in morphology due to the presence of a large first and second dorsal fin (Bass et al., 1975). Similar sized dorsal fins are found on Sand Tiger and Nurse Sharks, but these species swim more slowly (at a rate of $0.42ms^{-1}$ or $0.23\pm 0.77Ls^{-1}$ for Nurse Sharks; Castro and Rosa, 2005).

Lemon Sharks are characterized by a blunt head, flat ventral surface, very low heterocercal tail angle, an absent caudal fluke, and large pectoral fins (Thomson and Simanek, 1977). The TBF in Lemon Sharks increases with swimming speed and it has a higher TBF compared to some of the fastest swimming species of sharks (i.e. Mako Shark) (Graham et al., 1990). The TBF is a major kinematic factor that influences thrust and range of swimming speeds (Webb and Keyes, 1982). Critical swimming speeds (or the maximum aerobically sustained swimming speed) for juvenile Lemon Sharks averages at $0.71 \pm 0.03Ls^{-1}$ (or $\sim 0.55ms^{-1}$), while cruising speeds range around $0.19 \pm 0.01Ls^{-1}$, or $\sim 0.15ms^{-1}$ (Bouyoucos et.al, 2017). For adults, cruising speeds typically range between 0.33 and

$0.42Ls^{-1}$ (Gruber et al., 1988). Metabolic rate and cruising speeds for juvenile Lemon Sharks are directly related to tides and vary between tidal stages (Bouyoucos et al., 2017). In a controlled setting, the average metabolic rate of the Lemon Shark is $318mgkg^{-1}h^{-1}$ (Graham et al., 1990). Although previous studies of other shark species have provided evidence of the first dorsal fin's influence to enhance swimming efficiency (Thomson and Simanek, 1977; Lingham-Soliar, 2005; Mia et al., 2017), the hydrodynamic function of the second large dorsal fin of the Lemon Shark has not been previously studied.

3.0 Research Objectives

To better understand the hydrodynamic role of the second dorsal fin of a Lemon Shark (*Negaprion brevirostris*), we: i) evaluate the wake characteristics behind deceased and model Lemon Sharks with two large dorsal fins and compare these characteristics to those of a deceased Spinner Shark with one large dorsal fin and ii) examine what effect these wake characteristics have on the hydrodynamic forces acting on the sharks. This research is an experimental study performed in a laboratory using particle image velocimetry (PIV) to measure the flow in the wake behind both dorsal fins and behind the tail of deceased specimens and a flexible model shark. The deceased specimens consist of one juvenile Lemon Shark and one juvenile Spinner Shark. The model is made of silicon and is geometrically based on juvenile Lemon Shark measurements. The sharks are placed into a large recirculating flume individually, and two components of velocity over a two-dimensional area are measured using PIV. From the measured data, the shedding in the wake is characterized using proper orthogonal decomposition (POD) applied to vorticity fields. The spacing ratio is computed from the resulting POD modes to determine the stability of the street. The hydrodynamic forces thrust and drag are also computed. The drag is estimated using the velocity deficit in the wake (Goett, 1938) and a thrust model based on the evolution of a vortex street (Taylor et al., 2013) is also used to evaluate thrust. These quantities and comparisons provide insight into the shedding characteristics in the wake of Lemon Sharks and associated hydrodynamic forces, shedding light on the role of the second dorsal fin.

4.0 Experiments and Methodology

Measurements of Lemon Shark hydrodynamics were conducted in the flume located at the Environmental Fluids Laboratory (at CCU). The near wake flow was measured behind a modeled Lemon Shark, and deceased shark specimens (a Lemon Shark and a Spinner Shark). An overview of the experimental setup, the experiments conducted, and the methods that were used to analyze the measured data are explained below.

4.1 Shark Specimens

This study focuses on Lemon Sharks, with a second shark species used for comparison purposes. The species used include a juvenile Lemon Shark (*Negaprion brevirostris*), with a first and second dorsal fin almost equal in size and a juvenile first of year Spinner Shark (*Caracharhinus brevipinna*), with a large first dorsal fin and a small second dorsal fin (Thomson and Simanek, 1977; Webb and Keyes, 1982). The Spinner Shark was chosen for a point of comparison with the Lemon Shark as it is a species with one large dorsal fin that was readily available in the Myrtle Beach area. Each deceased shark was placed in the middle of the glass section of the flume individually (see Section 4.2), and suspended with fishing line, which prevented the shark from sinking (due to shark's negative buoyancy) and minimized flow disturbance of the mounting apparatus.

A flexible model Lemon Shark, as shown in Figure 8, was also used for experiments. The model enabled us to perform wake flow measurements in a more controlled manner. The

model unlike the dead specimen did not deteriorate in time, and in this way, may have been more representative of a live organism than the deceased shark. The model was fabricated using a 3D printed mold that was filled with silicon forming a flexible body (Kulkarni et al., 2017). The mold was created via SolidWorks, where a 3D drawing based on deceased juvenile Lemon Shark measurements was created (Figure 8.c) and inverted to generate a mold. The mold was 3D printed with onyx plastic and filled with a silicon-paint thinner mixture. To best replicate Lemon Shark flexibility the Young's modulus for the model was estimated and compared to deceased Lemon Shark flesh. The Young's modulus of the silicon was 1.1×10^3Pa, which was similar to that of sampled flesh (Young's modulus of 1.0×10^3Pa) and was in general agreement with the literature (Epps et al., 2009). The model was submersed in the flume and supported by a rod connected to a cross bar that spanned the width of the glass portion of the flume (Figure 8.b). The model was spray painted black to prevent reflection of laser light into the camera from the model (see Section 4.3). Data were collected in the near wake behind the first dorsal fin, second dorsal fin, and caudal fin.

(a) (b)

(c)

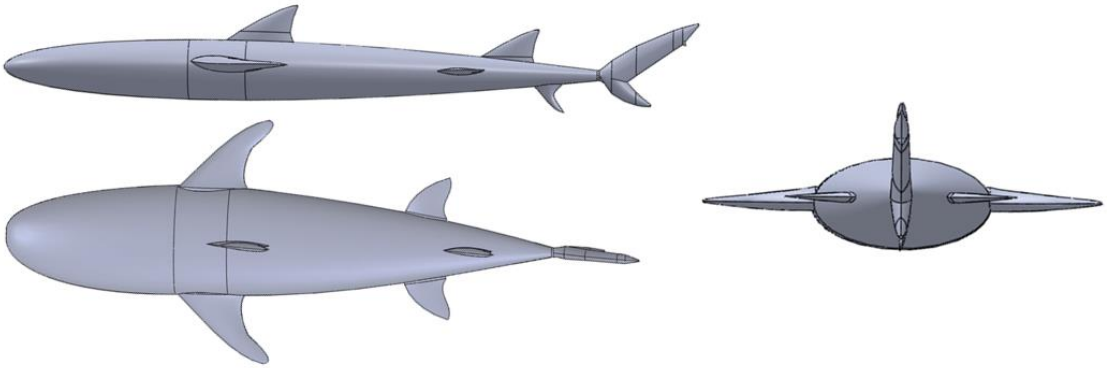

Figure 8: Illustration of the Lemon Shark model: (a) Top-down image of the silicon model created from the mold. (b) Spray painted shark model mounted in the flume with the PIV light sheet. (c) CAD model of the Lemon Shark, which was inverted into a mold and 3D printed.

4.2 Recirculating Open Water Channel (Flume)

The flume, shown in Figure 9, has two circular reservoirs on each end connected by an open channel that can hold over 6.5m³ of water, and flows from the left reservoir to the right reservoir in the figure. The total length of the flume is 20m with a cross section of 0.5m by 0.7m. The middle section of the channel is comprised of a 5m long glass section to allow optical access for flow measurements. A funnel and screen are placed at the outlet of the left reservoir to straighten the flow as it enters the channel. Flow restrictors (series of cylindrical pipes) are located just before the right reservoir (at the exit of the open channel) to maintain constant water level across the channel and prevent reflections from the downstream reservoir. The water is circulated by a low-pressure centrifugal pump, with flow rates ranging up to $0.048 m^3 s^{-1}$. The centrifugal pump is controlled by a variable frequency drive. The flow speed in the glass test section varies with pump frequency and water height. Flow speeds for the experiments were based on matching Reynolds numbers of each shark specimen with current literature (see Section 4.4).

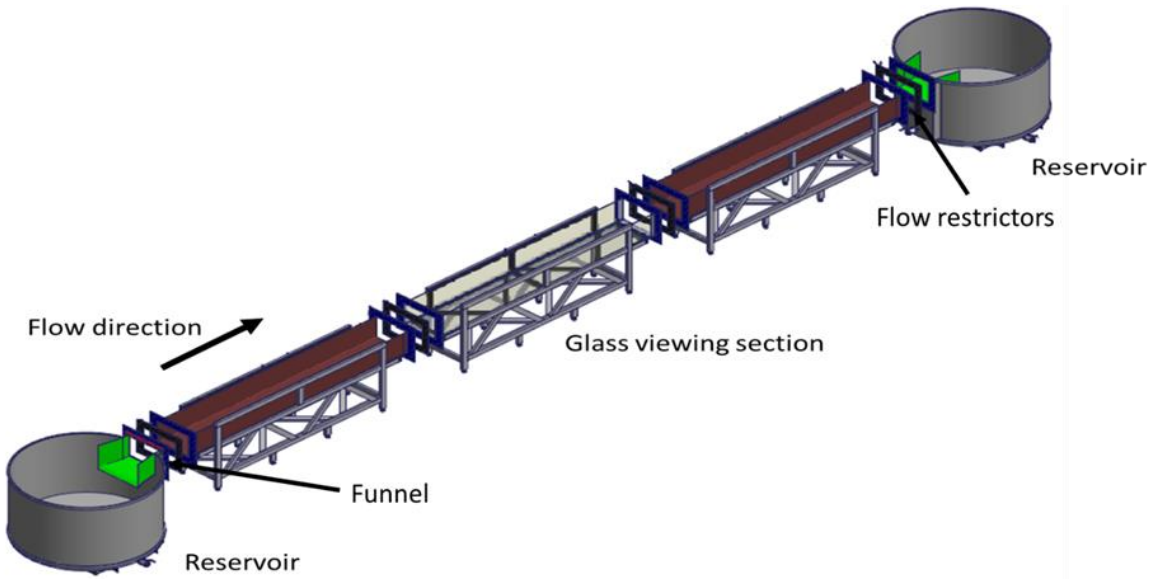

Figure 9: Schematic of flume in the Environmental Fluids Laboratory.

4.3 Particle Image Velocimetry Measurements

Experiments performed in the flume are measured using particle image velocimetry (PIV), a nonintrusive method that measures a two-dimensional velocity field (two components) over a two-dimensional area within the flow (Raffel et al., 1998; Adrian and Westerweel 2011). PIV was developed to examine turbulent flows using seeding particles, a light source (i.e., laser), and an imaging device (i.e., digital camera) to capture a series of images, which yield velocity vector maps. PIV measures velocity indirectly using seeding particles as tracers and measures their average displacement over a series of consecutive images (Adrian, 1991; Raffel et al., 1998). Seeding particles used for this experiment were hollow glass spheres that were neutrally buoyant and chemically inert, with an 11μm mean diameter (Melling, 1997). A dual pulsed laser and a series of optical lenses created a thin light sheet that illuminated the flow containing the seeding particles. Displacement of these particles were captured by a camera located perpendicular to the light sheet (Adrian, 1991; Melling,1997; Raffel et al.,1998). A TSI PowerView 29MP camera with a frame rate of 3.6fps and a dynamic range of 12bits produced an image of 6600 × 4400 pixels^2. Attached to the camera was a 200mm Nikon AF DC-Nikkor lens that increased the magnification and allowed for a more dynamic velocity range (Adrian, 1997). A 35mm extension tube was used to further increase magnification for all configurations that measured the wake behind dorsal fins. Spatial resolution and field of view of each experiment is described in Section 4.4 and a schematic of the experimental setup is shown in Figure 10.

A synchronizer for the camera and laser was used to set the timing between the laser pulses and the camera shutter to capture the image. The laser used for this study was a high-powered Neodymium doped: yttrium-aluminum-garnet (Nd-YAG) laser, which emitted a

monochromatic green laser pulse with power up to 140mJ/pulse (at a wavelength of 532nm). The laser beam traveled through a diverging cylindrical lens (focal length 12.7mm) and a converging spherical lens (focal length 500mm), which formed the light sheet (~1 mm thickness) and illuminated the particles (Figure 10). The light sheet formed in the center of the glass section of the flume in the wake behind the configuration and was oriented in the streamwise-spanwise plane at half the fin height (Figure 10). 600 image pairs were collected for each experiment to ensure statistical convergence.

Correlation analysis was used to compute the average displacement of tracer particles in 64×64 pixel^2 interrogation regions from one image set (pair of consecutive images), which divided by the time between images yielded an estimated velocity (Willert and Gharib, 1991; Westerweel et al., 1996). More specifically, particle displacements resulting from the correlation analysis were converted to physical units using:

$$V = \frac{x_*}{\Delta t} r \tag{1}$$

where V indicates velocity in either direction (i.e., u or w), x_* is the average pixel displacement in either the corresponding streamwise or spanwise direction, Δt is the time between images in an image pair, and r is the pixel-physical unit conversion obtained from images of a calibration target.

The data were cross correlated for each interrogation window with 50% overlap between adjacent windows (Willert and Gharib, 1991; Westerweel et al., 1996; Nogueira et al., 1997). The area of the image containing the fin was omitted in the correlation analysis by placing a mask over the dorsal fin and caudal fin during correlation and filtering. Any reflections from the glass were also masked and not included in the analysis. Valid

displacement estimates that resulted from the correlation analysis were above a signal-to-noise (SNR) ratio of 1.5, where the highest cross-correlation peak was the signal and the noise was the second highest cross-correlation peak.

Velocity vectors that passed the SNR threshold may still be erroneous, so additional filters were applied. Invalid results were removed using: a global filter and a local filter, and invalid vectors were replaced using the local median (Nogueira et al., 1997). The global filter removed vectors outside 3 standard deviations of the map mean displacement. The local filter compared individual vectors in the same area, and if a reference vector was greater or less than ± 2 pixels compared to the median displacement of its surrounding 5×5 vector neighboring area, it was replaced by the local median (Nogueira et al., 1997). Filtered vectors were replaced with the median displacement of the surrounding 5×5 neighborhood area using a recursive process that began at regions with the least vectors missing. Subsequently, the entire map was smoothed using a 5×5 top-hat averaging filter to ensure continuous derivatives (Nogueira et al., 1997). Error of the measured velocity was estimated to be ≈ 1.3% (Westerweel, 1997; Gurka, 2003; Stanek, 2018). An example of a resulting instantenous vector map can be seen in Figure 11.

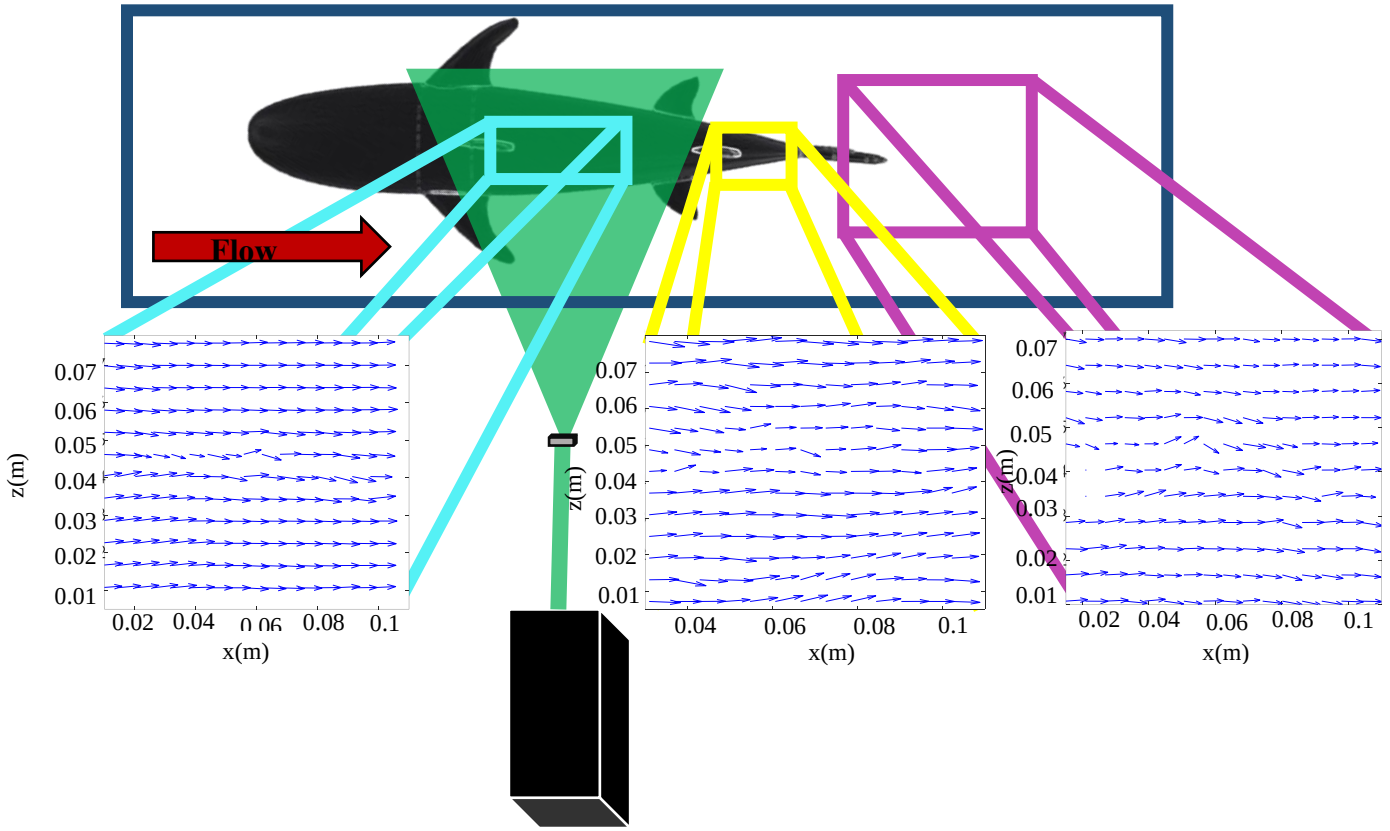

Figure 10: Top view of experimental setup within the flume. Three sampling (FOV) configurations are shown and resulting example vector maps. The presented vector maps are a subset of the measured data and do not represent the entire FOV.

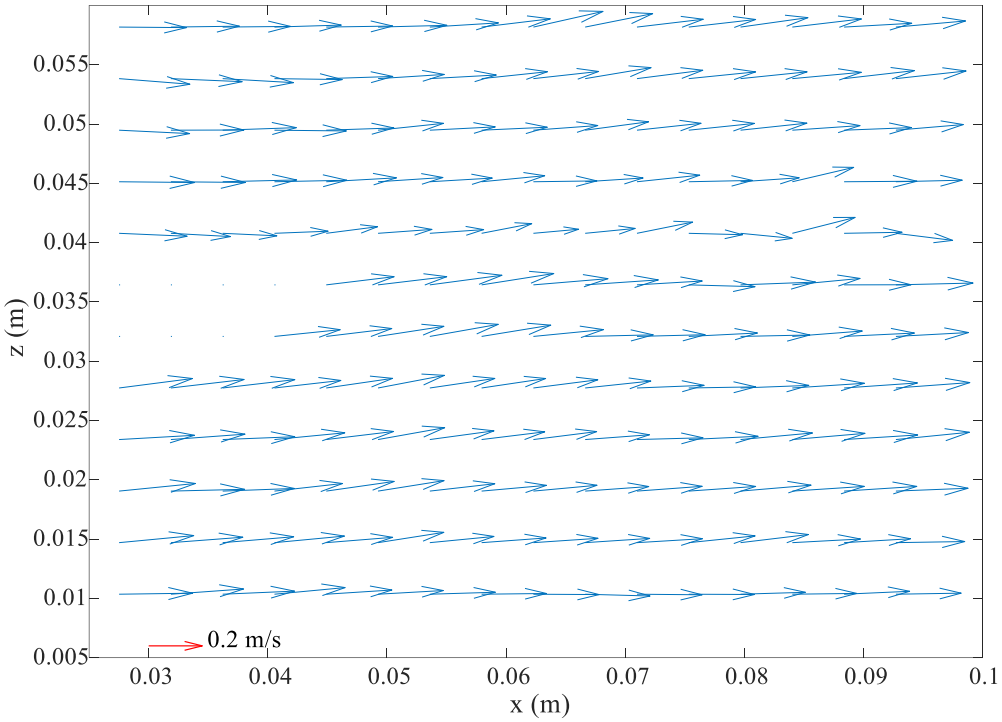

Figure 11: Example of an instantenous velocity vector map measured in experiment SS-1DF. A subsample of the vectors are shown for clarity.

4.4 Experiments

The matrix of experiments is listed in Table 1. As previously mentioned, three sharks were used for these experiments: two deceased shark specimens and one model. The flow velocity was ~0.2 ms^{-1} as this is a typical swimming speed of juvenile Lemon Sharks in vivo (Sundstörm et al., 2001). The flume was filled to a depth of 0.38m in the glass section of the flume to ensure that the specimen was fully submerged, and flow was at the required velocity. Reynolds number determines the ratio of inertial to viscous forces,

$$Re = \frac{U_\infty L_T}{\nu} \tag{2}$$

where U_∞ (~0.2ms^{-1}) is the freestream velocity in the streamwise direction (x), L_T is the total length of the shark and ν is the kinematic viscosity. The freestream velocity was estimated as the (spatial and ensemble) mean streamwise velocity over regions with approximately uniform flow over the spanwise direction. L_T = 0.93m for the Spinner Shark, L_T =0.61m for the deceased Lemon Shark, and L_T =0.5m for the model Lemon Shark, resulting in Reynolds numbers of 2×10^5, 1.3×10^5, and 1.1×10^5, respectively. These *Re* fall within the Reynolds number range for swimming fish: 10^3 (goldfish) to 10^8 (blue whale) (Webb, 1975; Eloy, 2012).

Data were collected in the wake behind the first dorsal fin, second dorsal fin, and caudal fin for the Lemon Shark and silicon Lemon Shark model (Figure 10), and data in the wake behind the first dorsal fin and caudal fin for the Spinner Shark were collected (Table 1). The light sheet was oriented in the spanwise-streamwise plane measuring *u* and *w*, where *u* is the streamwise velocity or the velocity in the *x* direction and *w* is the spanwise velocity or the velocity in the *z* direction. The light sheet was located at approximately half the fin

height in the vertical direction. The naming convention for experimental configurations was based on species and area of collection. For example, the configuration for the data collected behind the first dorsal fin of the Spinner Shark is named SS-1DF, where SS stands for Spinner Shark and 1DF stands for first dorsal fin. The size of the camera field-of-view (FOV), the time between image pairs (Δt), and conversion factor, *r*, for converting pixel displacements to physical distances (Eqn. 1) for each experiment is provided in Table 1.

Table 1: Matrix of experiments. All the experiments were performed in a water depth of 0.38 m and flow speed of ~0.2ms^{-1}.

Experiment	Configuration	Area of Data Collection	Δt (μm)	FOV (cm × cm)	r (cm/pixel)
SS-C	Spinner Shark	Behind the Caudal Fin	1500	18 × 10	3.2×10^{-3}
SS-1DF	Spinner Shark	Behind the First Dorsal Fin	550	7.5 × 6	1.5×10^{-3}
LS-C	Lemon Shark	Behind the Caudal Fin	800	20 × 14	1.6×10^{-3}
LS-1DF	Lemon Shark	Behind the First Dorsal Fin	650	9.6 × 5	1.5×10^{-3}
LS-2DF	Lemon Shark	Behind the Second Dorsal Fin	700	8 × 5	1.5×10^{-3}
MS-C	Lemon Shark Model	Behind the Caudal Fin	900	10 × 8	1.9×10^{-3}
MS-1DF	Lemon Shark Model	Behind the First Dorsal Fin	900	10 × 8	1.9×10^{-3}
MS-2DF	Lemon Shark Model	Behind the Second Dorsal Fin	900	10 × 8	1.9×10^{-3}

4.5 Analysis Methods

In order to evaluate the shedding characteristics in the wake and examine the effects these characteristics have on hydrodynamic forces, a proper orthogonal decomposition (POD) of the vorticity in the wake is applied to determine the presence of a vortex street. If a vortex street is identified, then wake characteristics including shedding frequency and Strouhal number, a non-dimensional number characterizing an organism's locomotion, are estimated from the street. The stability of the wake is also evaluated using Kronauer and von-Karman stability criteria. The measured velocity in the wake behind the models and deceased shark specimens are used to estimate the drag force and coefficient on the sharks. A non-traditional calculation of the thrust coefficient is also computed. These results give insight into the hydrodynamic function of the second dorsal fin of the Lemon Shark. The analysis methods used are described in detail below.

4.5.1 Wake Characterization

Proper orthogonal decomposition (POD) was originally described by Lumley (1970) to characterize turbulent features in flows. These features are extracted using orthogonal eigenfunctions (Berkooz et al., 1993; Holmes et al., 1996). To examine energy distribution of the flow in the wake for each configuration we look specifically at the vorticity in the flow. Vorticity is defined as the tendency of a fluid to rotate. We applied a POD to vorticity fields estimated from the measured velocities to visually extract a vortex street from the flow. POD divides the vorticity ensemble into a set of basis functions that optimally encapsulates the variance of the vorticity field,

$$\widehat{\omega}_y = \sum_{n=1}^{q} a_n \phi_n \tag{3}$$

where ϕ_n are the eigenfunctions of the vorticity, a_n are the coefficients correspondent to the eigenfunctions, and q is the total number of eigenfunctions (Gurka et al., 2006).

For this decomposition the snapshot method is used, where the number of snapshots (N=600) is significantly fewer than the number of data points in every snapshot (M~4272), or M>>N (Sirovich, 1987; Taylor, 2011). Instead of directly computing an autocorrelation tensor, the POD modes were calculated as a projection of the original vorticity fields onto an N × N symmetric matrix (**Q**). The decomposition of the matrix satisfies the equation,

$$\mathbf{QA} = \lambda\mathbf{A} \tag{4}$$

where **Q** is the symmetric matrix of the vorticity ensemble, λ are the eigenvalues, and the columns of **A** are the eigenvectors. The solution to Equation (4) is the discrete form of Equation (3). The results of the decomposition are modes (eigenfunctions), which are comprised of the right-hand side of Equation (4). The large-scale structures of the flow are identified using the dominant modes of the vorticity (Lumley, 1970; Gurka et al., 2006). The variance contribution of a given mode to the overall variance of the vorticity increases as the mode number decreases; therefore, lower modes (e.g., 1-10) are considered the dominant modes as they represent highly variant features in the flow.

Because vortex shedding is a dominant pattern in the flow, it can be identified in the dominant modes, if present. Here we define a vortex street by the lowest mode that shows four or more alternating positive and negative vortices as demonstrated in Figure 12.a (i.e., mode 4). To determine the vortex centers and convection speed of the street, the locations of maximum vorticity of the vortex street are identified using swirling strength. Swirling strength is a method to identify vortex cores using magnitude of complex eigenvalues of

the velocity gradient tensor (Chong et al., 1990; Hackett et al., 2011). The average streamwise velocity at these vortex cores (after removing the freestream velocity) is used to determine the convection speed of the vortex system. These vortex centers are also used to determine the vortex wavelength a and cross-stream distance b, as demonstrated in Figure 12.b. The vortex wavelength is defined as the distance between two positive or two negative vortices, and the cross-stream distance is defined as the vertical distance between adjacent vortices (i.e., one positive and one negative vortex) (Figure 12.b).

We estimate the Strouhal number, *St*, which is a non-dimensional number that can describe the oscillation or unsteadiness of the flow in the wake. Literature shows most swimming organisms fall within the range of 0.2-0.4 (Taylor et al., 2003; Eloy, 2012). The *St* number is defined:

$$St = \frac{b}{U_\infty} f \tag{5}$$

where f is the shedding frequency:

$$f = \frac{U_w}{a} \tag{6}$$

and U_w is the wave speed of the vorticies,

$$U_w = U_s + U_\infty \tag{7}$$

with U_s defined as the speed of the vortex system, or the convection speed of the vortices (Taylor et al., 2013).

To determine if the street is stable, the results are compared to the von-Karman stability criteria, which states that a vortex street is stable when $b/a \approx 0.28$ (Bearman, 1967). The

Kronauer stability criteria is also evaluated, which connects the hydrodynamic forces acting on the body to the characteristics of the wake (Bearman, 1967; Kronauer, 1964),

$$\left(\frac{\partial C_D}{\partial (b/a)}\right)_{\frac{U_s}{U_\infty}=constant} \approx 0 \tag{8}$$

where C_D is the drag coefficient. If the spacing ratio of the vortex street in the wake and drag coefficient (see Section 4.5.2) exhibit the relationship shown in Equation (8), then the vortex street is considered to be stable and the drag coefficient minimized with respect to the vortex street pattern (Bearman, 1967). During steady swimming (simulated in this study), the thrust and drag are acting equally on the body, so we can substitute C_T for the drag coefficient C_D in Equation (8), which, by corollary, determines if C_T is maximized by the vortex street pattern (i.e., when it is stable). A nontraditional method is used to compute C_T as explained in Section 4.5.2.

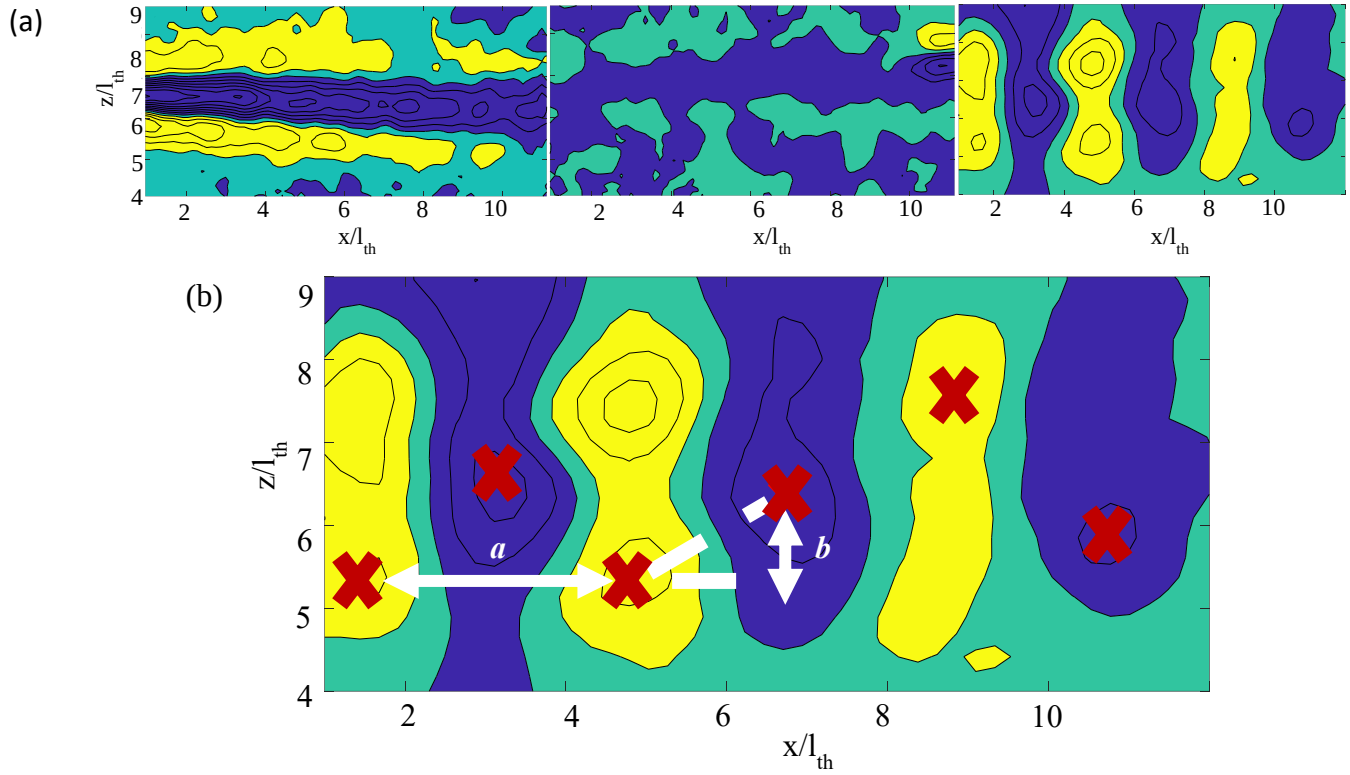

Figure 12: Example of the (decomposition) modes behind the 1st dorsal fin of the Lemon Shark: a.) POD modes 2- 4 (read from left to right) of vorticity for experiment LS-1DF and b.) Mode 4 which was identified to be the lowest mode that contains a vortex street shown with vortex centers (red x), vortex wavelength, a, and cross stream distance, b, denoted. Streamwise and spanwise locations are normalized with l_{th}, the maximum diameter of the specimen.

4.5.2 Hydrodynamic Forces

Thrust, drag, lift, and buoyancy are the main forces acting on a swimming shark. This study focuses on thrust and drag. Using mean streamwise velocity spanwise profiles measured in the wake by PIV, the drag force and drag coefficient are computed. The drag was estimated from the momentum equation based on Goett (1939) who developed an expression for drag based on the velocity deficit in the wake for steady flows:

$$D = \rho \int_0^h \bar{u}(U_\infty - \bar{u})dz \tag{9}$$

where ρ is the density of the water, h is the width of the wake in the spanwise plane, and $\bar{u}(z)$ is the mean streamwise velocity profile (in the spanwise direction) of the wake. Dh_f is computed, where h_f is the height of the fin (0.07m for the Spinner, 0.04m for the Lemon, and 0.03m for the model Lemon Shark), to estimate the drag force over the total area of the dorsal fin. For measurement configurations behind the caudal fin, h_f is replaced with l_{th}, the maximum diameter of the specimen (0.15m for the Spinner Shark, 0.11m for the Lemon shark, and 0.09m for the model Lemon Shark). The drag force was used to compute the drag coefficient,

$$C_D = \frac{Dh_f}{\rho A U_\infty^2/2} \tag{10}$$

where A is the wetted area, which was estimated by:

$$A = 0.4(L_T)^2 \tag{11}$$

with L_T as the total length and 0.4 as a standard non-dimensional factor used within the literature (Sagong et al., 2013; Kempf and Neu, 1932; Harris, 1936; Sundnes, 1963).

The coefficient of thrust was computed using the wake characteristics described in Section 4.5.1. Specifically, the thrust coefficient of the vortex street is estimated as (Taylor, et al. 2013):

$$C_T = \frac{4}{\pi}\left(\frac{U_s}{U_\infty}\right)^2 \left[\left(\frac{U_\infty}{U_s} - 2\right)\frac{\pi b}{a} coth\frac{\pi b}{a} + \coth^2\frac{\pi b}{a}\right] \quad (12)$$

The thrust coefficient of the vortex street enables estimates of thrust in the absence of undulation (Taylor, et al. 2013). Because the body of all three specimens are placed at a 0° angle of attack and the body is not moving, thrust and drag are equivalent forces acting on the body. Using different methods to compute the coefficients of these forces, we can evaluate the accuracy of this non-traditional method of computing the thrust coefficient given by Equation (12).

5.0 Results

Results from performed experiments described by the methodology in the previous section are presented below in the order which water flows across the body of a forward-moving shark. Results of the wake characteristics and hydrodynamic forces behind the dorsal fins and caudal fin for each specimen are described. The mean velocity distributions are shown via vector and contour maps to qualitatively examine the wake behind each configuration. The mean streamwise velocity spanwise profiles examine the downstream recovery of the wake along the spanwise direction and are compared between specimens. Shedding characteristics are examined from the POD of vorticity, which is computed to identify the presence of a vortex street from the dominant modes and if found, the spacing ratio and wake stability are evaluated and compared between configurations. From the shedding characteristics, specifically the spacing ratio, the thrust coefficient is estimated. The drag force and drag coefficient were computed from the mean streamwise velocity spanwise profiles. These results enable a comprehensive examination of the wake characteristics behind the dorsal and caudal fins, including drawing connections between these characteristics and the resulting hydrodynamic forces acting on the specimens; thus enabling insight into the role of the second dorsal fin of the Lemon Shark.

5.1 First Dorsal Fin

5.1.1 Wake Characteristics

The wake behind the first dorsal fin was studied for three specimens: a deceased juvenile Lemon Shark, a deceased juvenile Spinner Shark, and a flexible Lemon Shark model. Ensemble averaging of the instantaneous velocity vector maps acquired using the PIV technique described in Section 4.3 (Figure 10) yields mean velocity vector maps shown in Figure 13 for SS-1DF, LS-1DF, and LMS-1DF. These mean velocity vector maps provide an unclear representation of the wake, so a contour map of $\bar{u}$ and $\bar{w}$ are shown in Figure 14. Here, the velocity is converted to body lengths per second (Ls^{-1}) and *x* and *z* coordinates are normalized by the maximum diameter of each specimen (l_{th}). Mean $\bar{u}$ velocity contours show a velocity deficit in the wake for all three specimens (Figure 14.a-c). SS-1DF presents the smallest decrease in velocity in the wake, with a flow decrease of $0.08Ls^{-1}$ (Figure 14.a). LS-1DF and LMS-1DF show similar streamwise velocity wake contours with a maximum decrease in flow of $0.14Ls^{-1}$ (Figure 14.b, Figure 14.c).

Mean spanwise velocity contours show qualitatively similar patterns for all first dorsal fin configurations (Figure 14.d-f). The wake behind LS-1DF appears to be dominated by negative $\bar{w}$ velocity for z/l_{th} > ~0.4 positions (Figure 14.e). LMS-1DF most clearly shows a positive and negative *w* velocity on each side of the fin, indicating flow convergence immediately behind the fin (Figure 14.f).

Mean streamwise velocity spanwise profiles at various downstream positions normalized by l_{th} are shown in Figure 15 for the wake behind the first dorsal fin. All three configurations show a deficit in the wake behind the first dorsal fin with a 15%-30% decrease in flow speed from the freestream. SS-1DF and LMS-1DF show a larger decrease

in velocity compared to LS-1DF. SS-1DF and LS-1DF show a substantial but not full recovery of the velocity deficit by x/l_{th}=0.3 (Figure 15). LMS-1DF appears to show little recovery at the same distance, indicating that the wake takes longer to recover. It is unclear as to why the recovery differs.

Following Section 4.5.1, the POD of vorticity is computed from measured PIV data to examine the shedding characteristics in the wake. The cumulative relative energy of the modes versus the number of modes for all configurations is shown in Figure 16. SS-1DF and LS-1DF show similar convergence, with 90% of the energy represented by the first 80 modes, while LMS-1DF reaches 90% energy by the first 100 modes (Figure 16). The large number of modes to represent 90% of the variance (energy) has been observed in computational fluid dynamics (CFD) of small-scale flows, with a domain size like the FOV in this study (Hekmati et al., 2011).

The POD modes are used to identify the presence of a vortex street, where the first mode represents the most variance or energy of the vorticity. As stated in section 4.5.1 the dominant mode is typically chosen from the first 10 modes as they represent the most variance from the data. For this study, we define a dominant mode as the lowest mode that presents a vortex street, or four or more alternating positive and negative vortices. The dominant POD mode presenting this vortex street is shown in Figure 17. SS-1DF, LS-1DF, and LMS-1DF show a vortex street in the same lowest POD mode (mode 4) (Figure 17). Consecutive modes 1-6 for each specimen are shown in Figures 18(a-f), 19(a-f), and 20(a-f). A double shear layer can be seen in mode 1 for all three specimens, representative of the mean vorticity of a wake flow (Figure 18.a, Figure 19.a, Figure 20.a).

From the POD modes described in Section 4.5.1 the presence of a vortex street is determined behind the wake of each configuration. If a street is present, then the thrust coefficient can be computed from the spacing ratio of the dominant mode using Eqn. 12 (Section 4.5.2). The spacing ratio is computed from these vortex street modes by identifying the center of vortex circulation based on swirling strength and then estimating the cross-stream distance (*b*) and vortex wavelength (*a*) (Figure 12). The spacing ratio for all dorsal fin configurations is provided in Table 2, which range from 0.1 and 0.26. Based on these spacing ratios the von-Karman stability criteria is most closely satisfied for LS-1DF, indicating a stable vortex street is associated with LS-1DF. Both SS-1DF and LS-1DF have *St* numbers within the 0.2-0.4 range, indicating efficient swimming (Table 2). Strouhal number for fish fins is limited, but a robotic oscillating pectoral fin yields a *St* number of 0.26 (Bandyopadhyay et al., 2008), a similar *St* as LS-1DF.

To summarize, the flow converges behind 1DF for both the Lemon and Spinner Shark. Based on the mean streamwise velocity spanwise profiles, the wake from the first dorsal fin has no direct effect on the overall wake of the body, as the flow is almost fully recovered at a distance equal to 1/3 of the maximum diameter of the body. For the specimens in this study, this dimensional distance is roughly 3cm. The distance from the base of the first dorsal fin to the base of the second dorsal fin is 9cm for the model and 11cm for the deceased Lemon Shark specimen. Therefore, the vortex street developed from the first dorsal fin has little effect on the upstream flow prior to the second dorsal fin. This result is consistent for both species.

Table 2: Wake characteristics based on POD analysis applied to the vorticity field; vortex wavelength, a, cross stream distance, b, spacing ratio, $\frac{b}{a}$, and Strouhal number, St for dorsal fin configurations.

Experiment	a (m)	b (m)	$\frac{b}{a}$	St
SS-1DF	0.014	0.003	0.21	0.20
LS-1DF	0.015	0.004	0.26	0.30
LMS-1DF	0.019	0.002	0.11	0.10
LS-2DF	N/A	N/A	N/A	N/A
LMS-2DF	0.020	0.002	0.10	0. 10

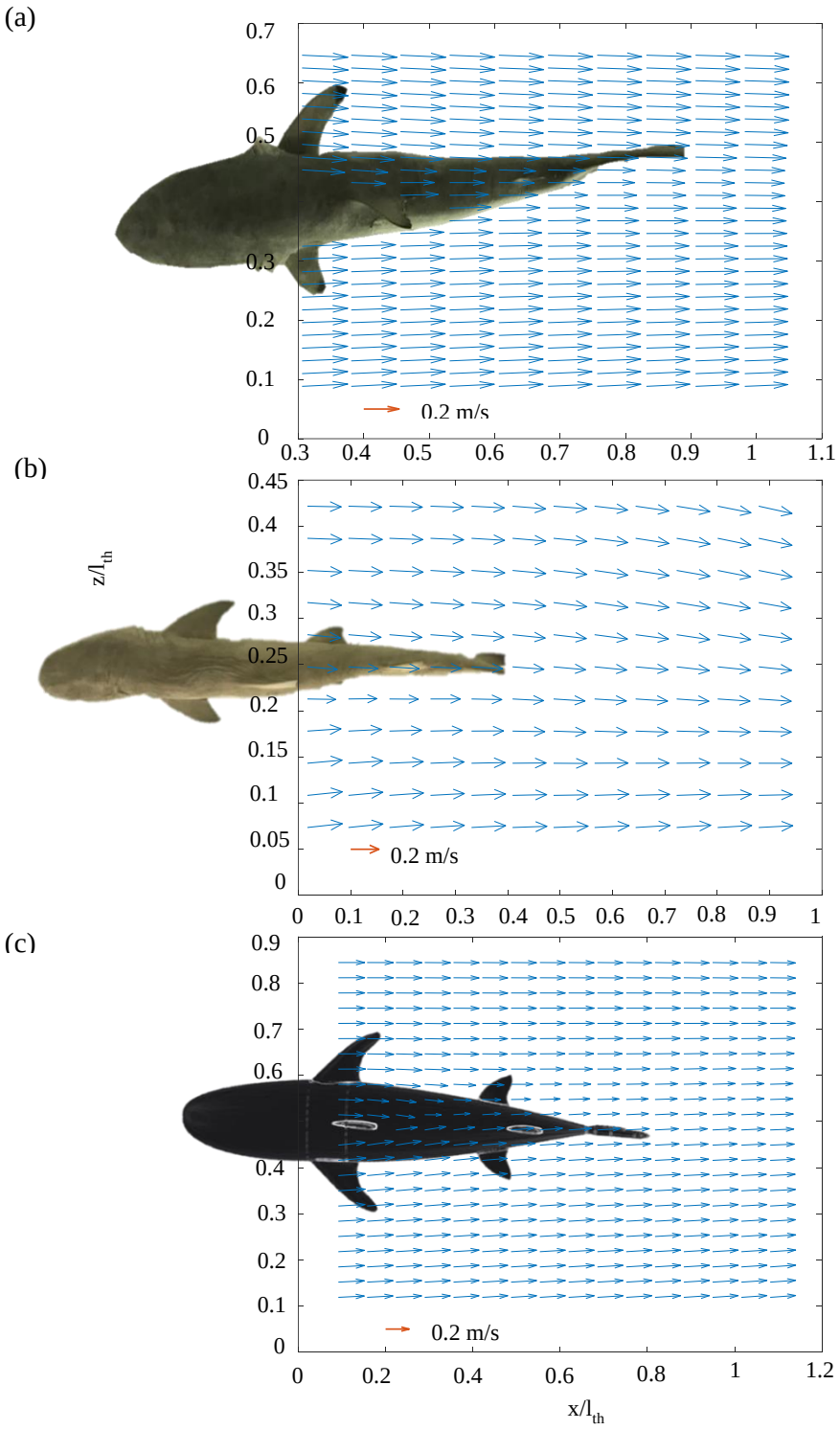

Figure 13: Mean velocity vector maps for SS-1DF (a), LS-1DF (b), and LMS-1DF (c). The spanwise and streamwise positions are normalized by the maximum diameter of the body (l_{th}).

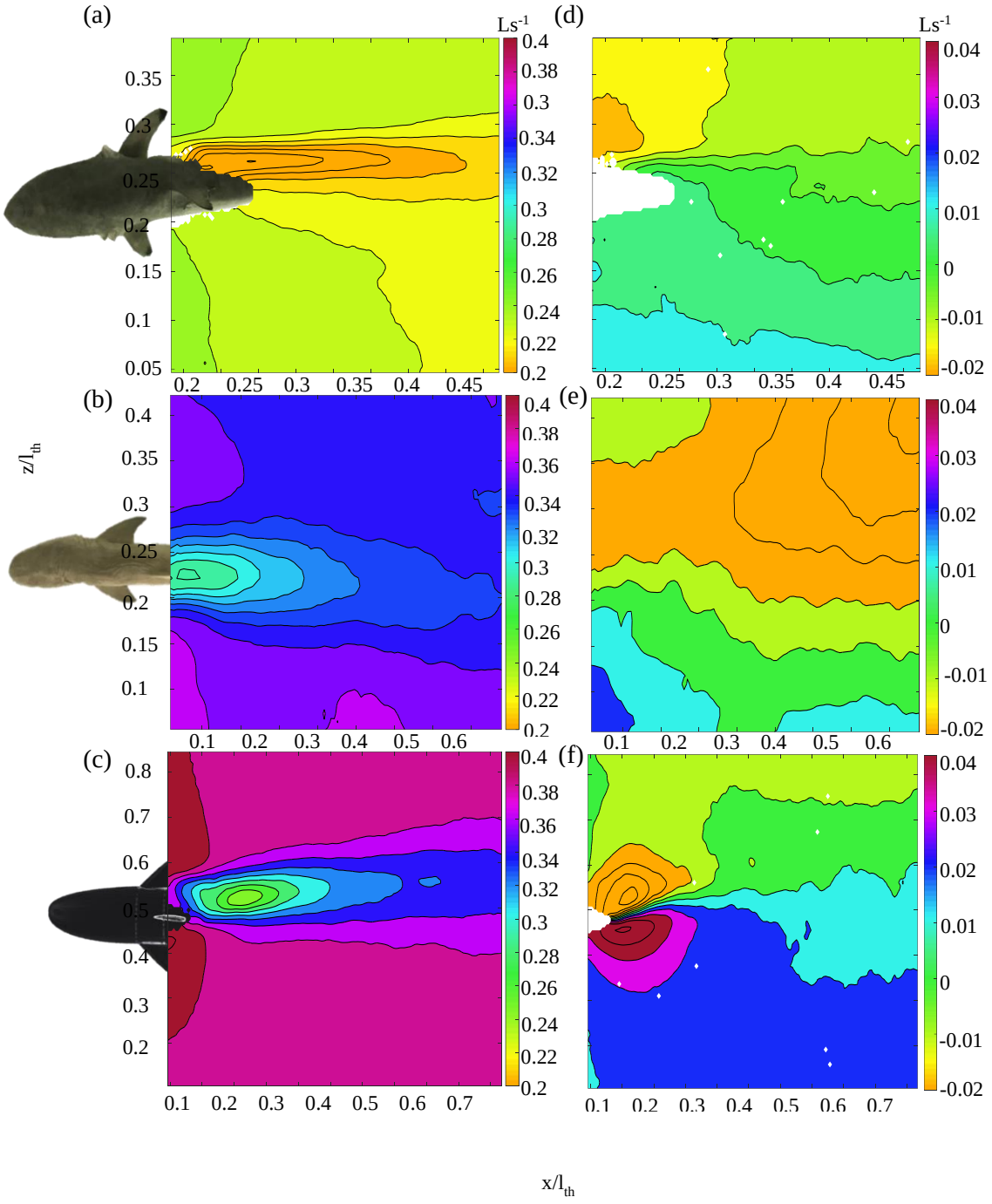

Figure 14: Mean velocity contours for streamwise velocity (a-c) and spanwise velocity(d-f) directions for SS-1DF (a,d), LS-1DF (b,e), and LMS-1DF (c,f).

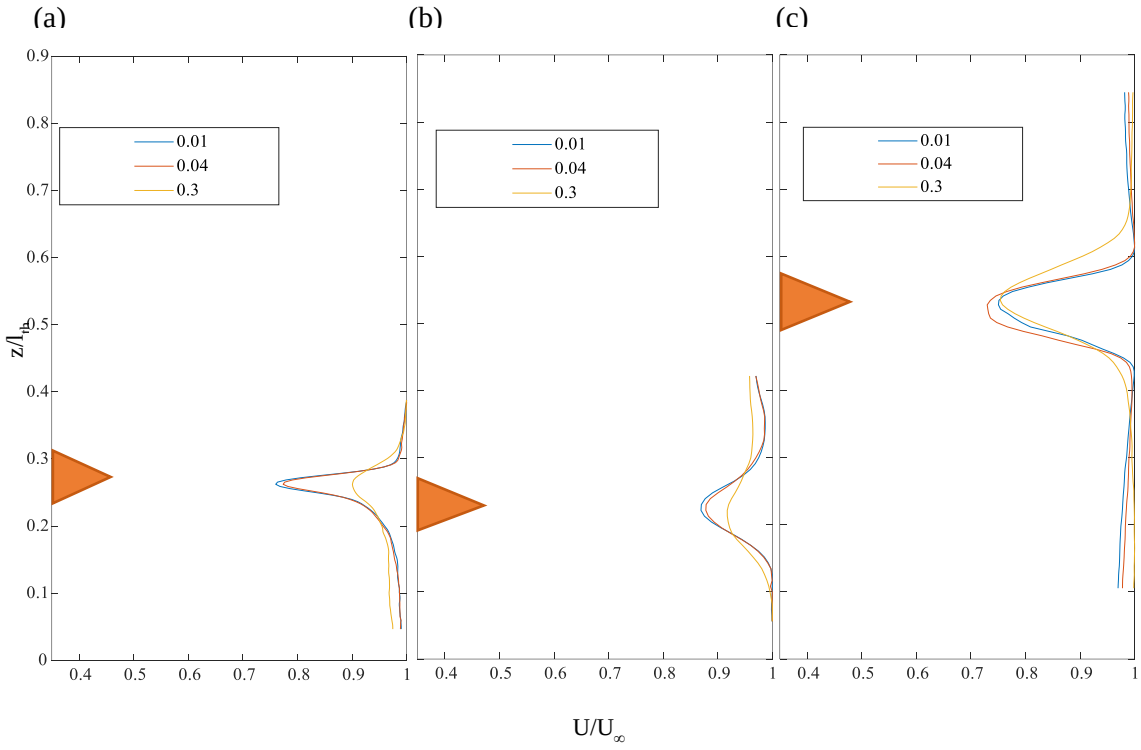

Figure 15: Mean streamwise velocity spanwise profiles for SS-1DF (a), LS-1DF (b), and LMS-1DF (c) at various normalized downstream positions (x/l_{th}; see legend). An orange triangle marks where the tip of the caudal fin is located.

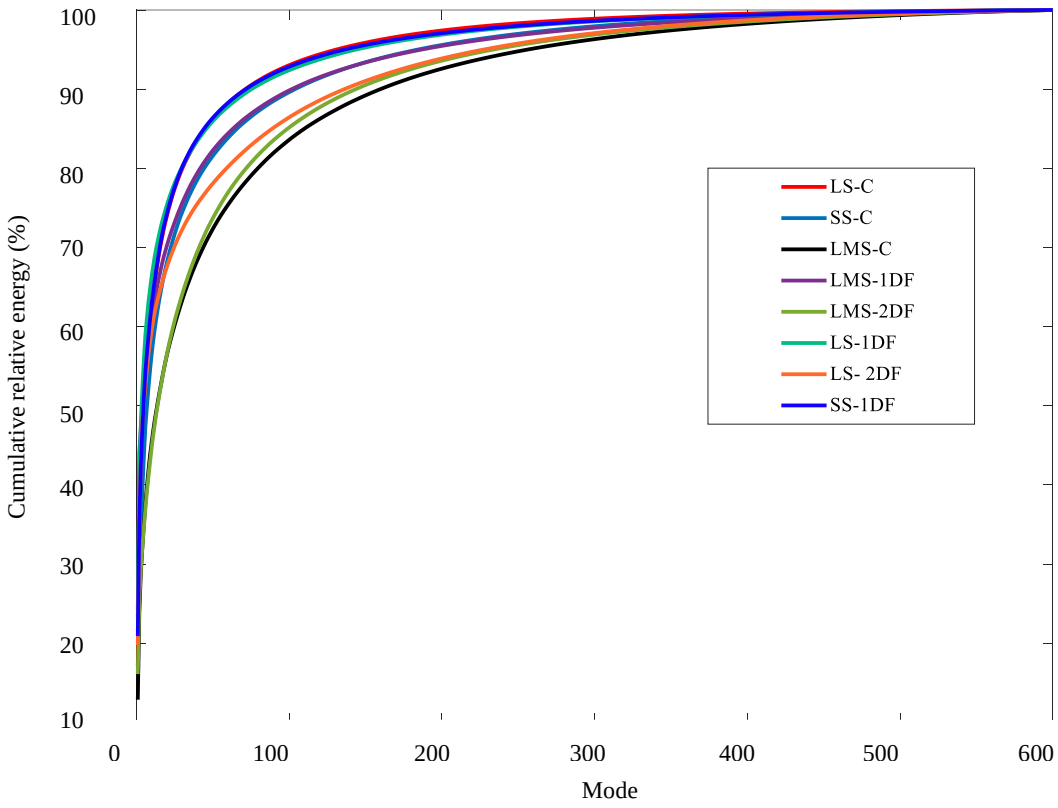

Figure 16: Cumulative relative energy versus number of POD modes for all configurations (see legend).

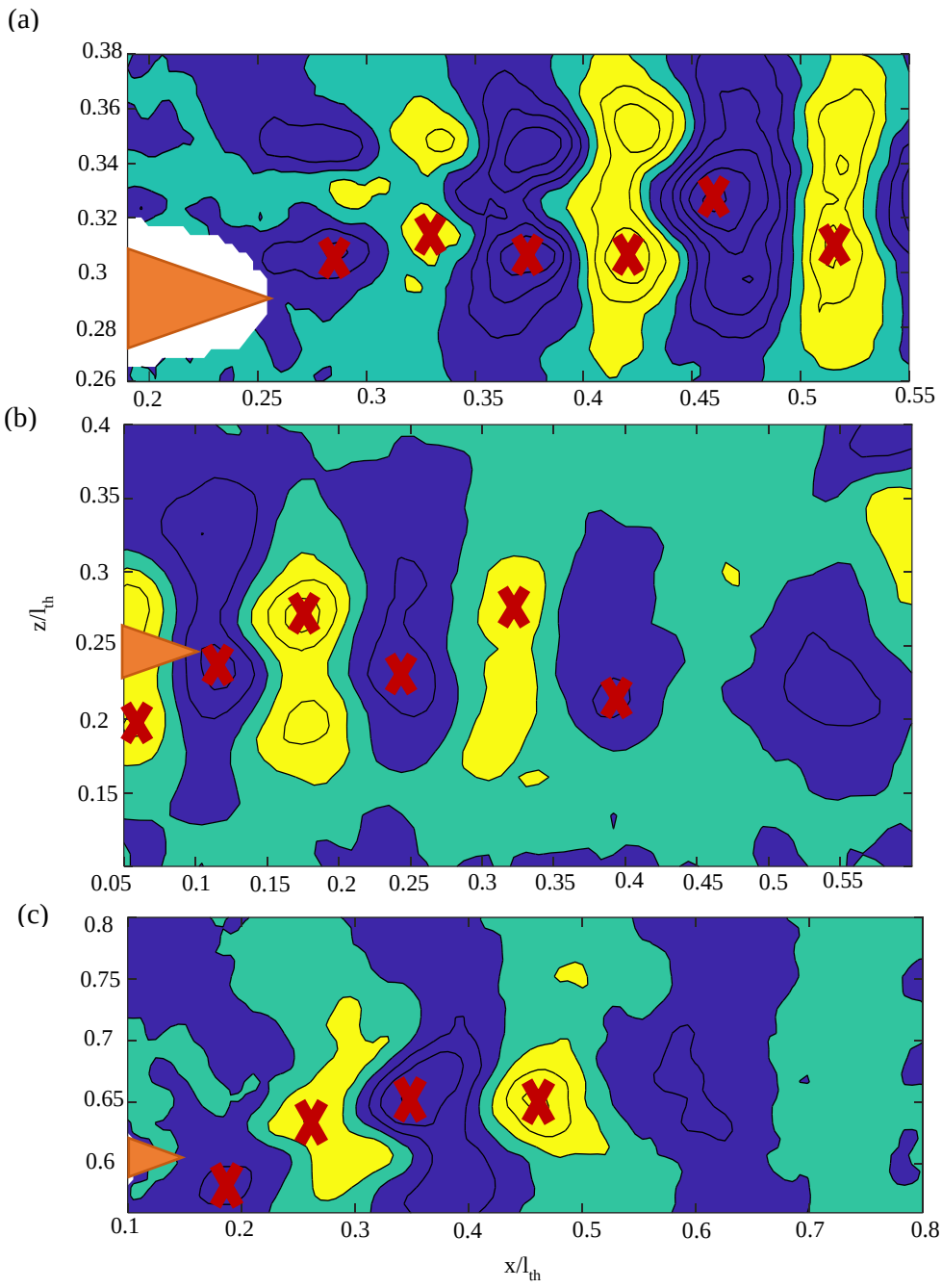

Figure 17: Lowest POD mode exhibiting a vortex street for SS-1DF (a), LS-1DF (b), and LMS-1DF (c); mode 4. The red "x" indicates the center of circulation for each vortex based on swirling strength. An orange triangle marks where the tip of the fin is located.

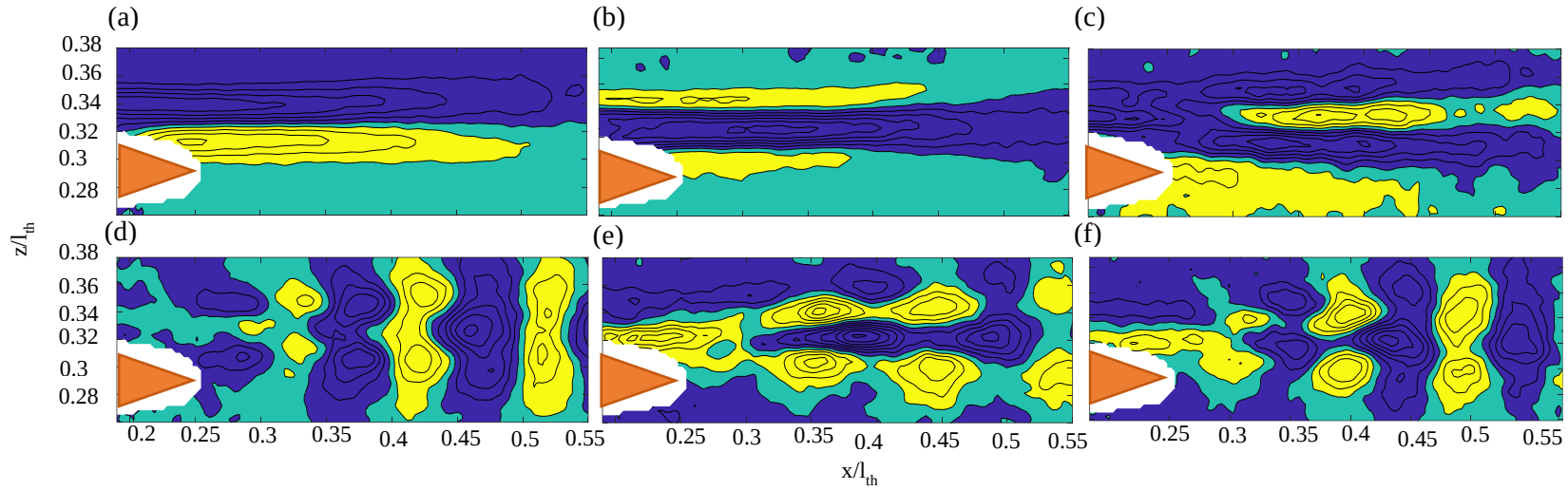

Figure 18: POD modes 1-6 (a-f, respectively) for SS-1DF. An orange triangle indicates where the tip of the fin is located.

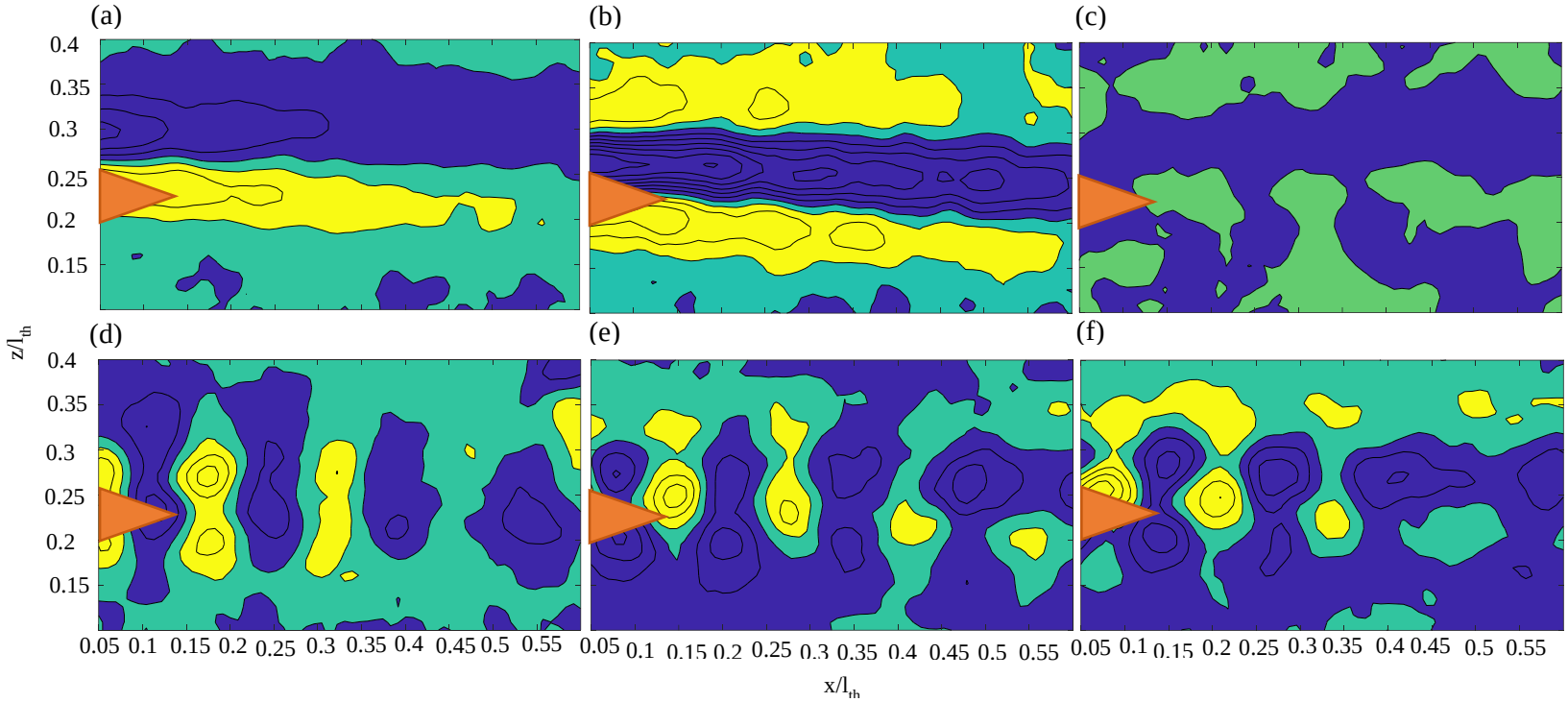

Figure 19: POD modes 1-6 (a-f, respectively) for LS-1DF. An orange triangle marks where the tip of the fin is located.

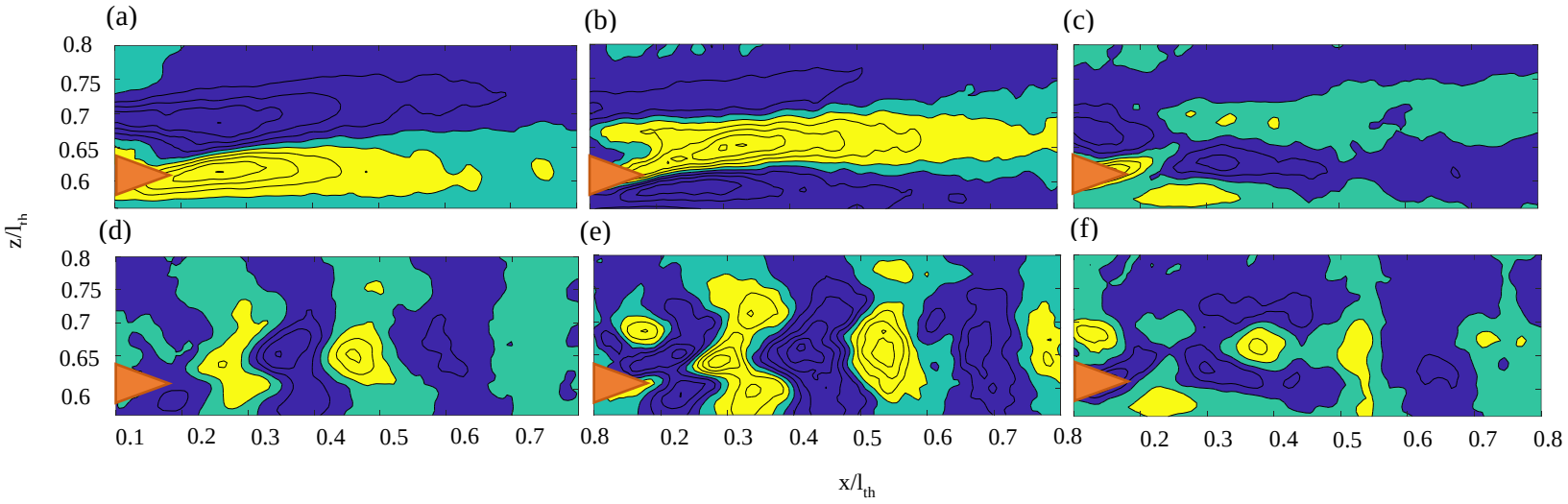

Figure 20: POD modes 1-6 (a-f, respectively) for LMS-1DF. An orange triangle marks where the tip of the fin is located.

5.1.2 Hydrodynamic Forces

The drag force is computed from the wake velocity deficit as described in Section 4.5.2 (Eqn. 9) and used to compute the drag coefficient for each experiment (Eqn. 10). The results of the hydrodynamic forces are shown in Table 3. The mean streamwise momentum spanwise deficit, which is the velocity deficit multiplied by $\bar{u}$, is shown for the first dorsal fin in Figure 21. LMS-1DF has the widest deficit, covering a non-dimensional distance of 2.2×10^{-2}, and SS-1DF has the largest peak momentum deficit at ~$6.0\times10^{-3}m^2s^{-2}$ (Figure 21). From the momentum deficit the drag and C_D is computed. Despite visual differences of the momentum deficit, C_D behind the first dorsal fin show similar drag coefficient results for LS-1DF, LMS-1DF, and SS-1DF (Table 3). This result is easily explained by the differing momentum deficit spanwise widths. A smaller magnitude deficit over a wider region can generate the same integral (Eqn. 9) as a narrow region with a large deficit. Therefore, no significant difference was found between the Lemon Shark and Spinner Shark in terms of drag behind the first dorsal fin.

From Section 4.5.2 a non-traditional computation of the thrust coefficient (Eqn. 12) is used to compare to drag coefficient results. Results show thrust coefficient values behind the first dorsal fin (Table 3) are higher compared to corresponding drag coefficients. Despite differences in values for C_T and C_D, results for C_T are similar for all three 1DF configurations, indicating the first dorsal fin produces the same amount of drag and thrust coefficients for both the Spinner and Lemon Shark. Results of C_T and C_D are not equal as presumed, which could be due to different areas used to compute the coefficients (area of the wake behind the body and wetted surface area respectively).

Table 3: Fin measurements (h_f and width), maximum diameter (l_{th}),total wetted surface area (A), thrust coefficient (C_T), total drag force (Dh_f), and drag coefficient (C_D) for all configurations.

Experiment	h_f (m)	Fin width(m)	l_{th}(m)	A(m^2)	C_T	Dh_f (N)	C_D
SS-C	1.6×10^{-1}	1.2×10^{-2}	1.5×10^{-1}	4.5×10^{-1}	4.0×10^{-2}	2.1×10^{-1}	3.0×10^{-2}
SS-1DF	7.0×10^{-2}	6.5×10^{-3}	1.5×10^{-1}	4.5×10^{-1}	2.1×10^{-1}	5.0×10^{-2}	4.0×10^{-3}
LS-C	1.1×10^{-1}	8.0×10^{-3}	1.1×10^{-1}	4.5×10^{-1}	8.0×10^{-2}	7.0×10^{-2}	1.0×10^{-2}
LS-1DF	4.0×10^{-3}	6.0×10^{-3}	1.1×10^{-1}	2.9×10^{-1}	2.1×10^{-1}	2.0×10^{-2}	3.0×10^{-3}
LS-2DF	3.5×10^{-2}	3.0×10^{-3}	1.1×10^{-1}	2.9×10^{-1}	N/A	3.0×10^{-2}	7.0×10^{-3}
LMS-C	7.0×10^{-2}	6.0×10^{-3}	9.0×10^{-2}	2.4×10^{-1}	8.0×10^{-2}	5.0×10^{-2}	1.6×10^{-2}
LMS-1DF	3.3×10^{-2}	5.0×10^{-3}	9.0×10^{-2}	2.4×10^{-1}	2.0×10^{-1}	2.0×10^{-2}	4.0×10^{-3}
LMS-2DF	3.3×10^{-2}	5.0×10^{-3}	9.0×10^{-2}	2.4×10^{-1}	1.4×10^{-1}	3.0×10^{-2}	8.0×10^{-3}

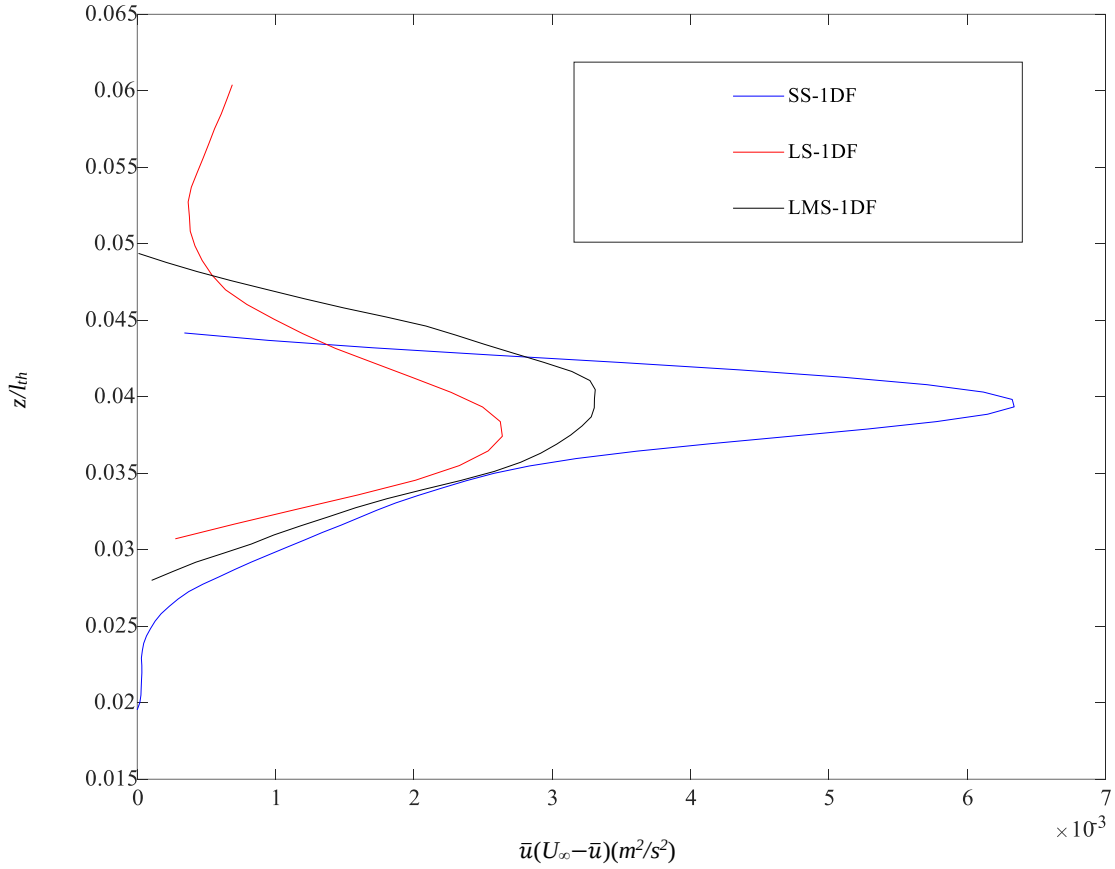

Figure 21: Mean streamwise momentum deficit vs. non dimensional spanwise distance for SS-1DF, LS-1DF, and LMS-1DF (see legend).

5.2 Second Dorsal Fin

5.2.1 Wake Characteristics

Mean vector maps and velocity contours behind the second dorsal fin are shown in Figures 22 and 23 respectively for the Lemon Shark (LS-2DF, LMS-2DF). Similar to results of the first dorsal fin configurations mean *u* velocities show a deficit in the flow behind the second dorsal fin of the Lemon Shark (Figure 23.a, 23.b). Unlike the first dorsal fin configurations, farther downstream in Figure 23.a, another deficit appears to form as the flow approaches the caudal fin, which is located outside the FOV at x/l_{th}= 0.9 (Figure 23.a). This deficit does not appear in the model due to the vertical position of the caudal fin. Meaning the upper lobe of the caudal fin of the deceased Lemon Shark intersected the light sheet, but the caudal fin of the model did not, explaining the lack of the second deficit. Mean *w* velocity contours shows differences in the spanwise flow between the model and deceased Lemon Shark (Figure 23.c, 23.d). Differences between the model and deceased specimen could be the result of the preservation quality of the deceased Lemon Shark, making precise alignment of the Lemon Shark in the streamwise direction difficult.

When comparing the mean streamwise velocity spanwise profiles in Figure 24 of LMS-2DF and LS-2DF, both show a larger deviation from the freestream compared to the first dorsal fin configurations, with over a 40% decrease from the freestream. LMS-2DF shows a quicker recovery of the deficit compared to LS-2DF, and both configurations depict a maximum recovery between 65% and 80% at a distance over half the maximum diameter of the body (Figure 24). This result provides evidence that the second dorsal fin has an impact on the overall wake of the body for the Lemon Shark, as the second dorsal fin is

located directly in front of the peduncle region and the wake takes further distance to recover than flow between the first and second dorsal fin.

For second dorsal fin configurations, the convergence of the cumulative relative energy across the number of modes is depicted in Figure 16. 90% of the variance of vorticity is represented by the first 135 modes for LS-2DF and the first 150 modes for LMS-2DF (Figure 16). Compared to the first dorsal fin configurations, it takes 50-55 more modes to reach 90% relative energy. These additional modes could suggest of a more complex flow regime in the wake behind the second dorsal fin.

POD results in the wake behind the second dorsal fin of the Lemon Shark do not show a vortex street in modes 1-6 as shown in Figures 25 and 26. As stated previously, the second dorsal fin is directly in front of the peduncle region, which connects the caudal fin to the rest of the body. The upper lobe of the caudal fin is positioned at an angle above the body, which can lead to a reverse flow of fluid between the second dorsal fin and the caudal fin. Hence, this flow reversal could be a plausible reason that prevents the formation of a vortex street, as the wake from the second dorsal fin would intersect with the reversed flow in front of the caudal fin.

The second dorsal fin of the Lemon Shark presents interesting results as the wake is larger compared to the first dorsal fin and takes a longer distance to recover despite its similar size. This result gives evidence that the overall wake could be impacted by the presence of this second dorsal fin, as the distance between the second dorsal fin and the base of the caudal fin is roughly 2cm and the wake extends to a distance equal to 6/10 of the maximum diameter of the body, which is between 5 and 6cm. POD modes also present intriguing results as no vortex street can be seen in the wake behind the second dorsal fin. Because

there is no street present, which indicates that the wake is not organized, there could be strong mixing behind the second dorsal fin. As discussed previously, the wake behind 2DF could interact with the recirculation zone preceding the caudal fin, which could also explain why a vortex street doesn't form behind the Lemon Shark's second dorsal fin.

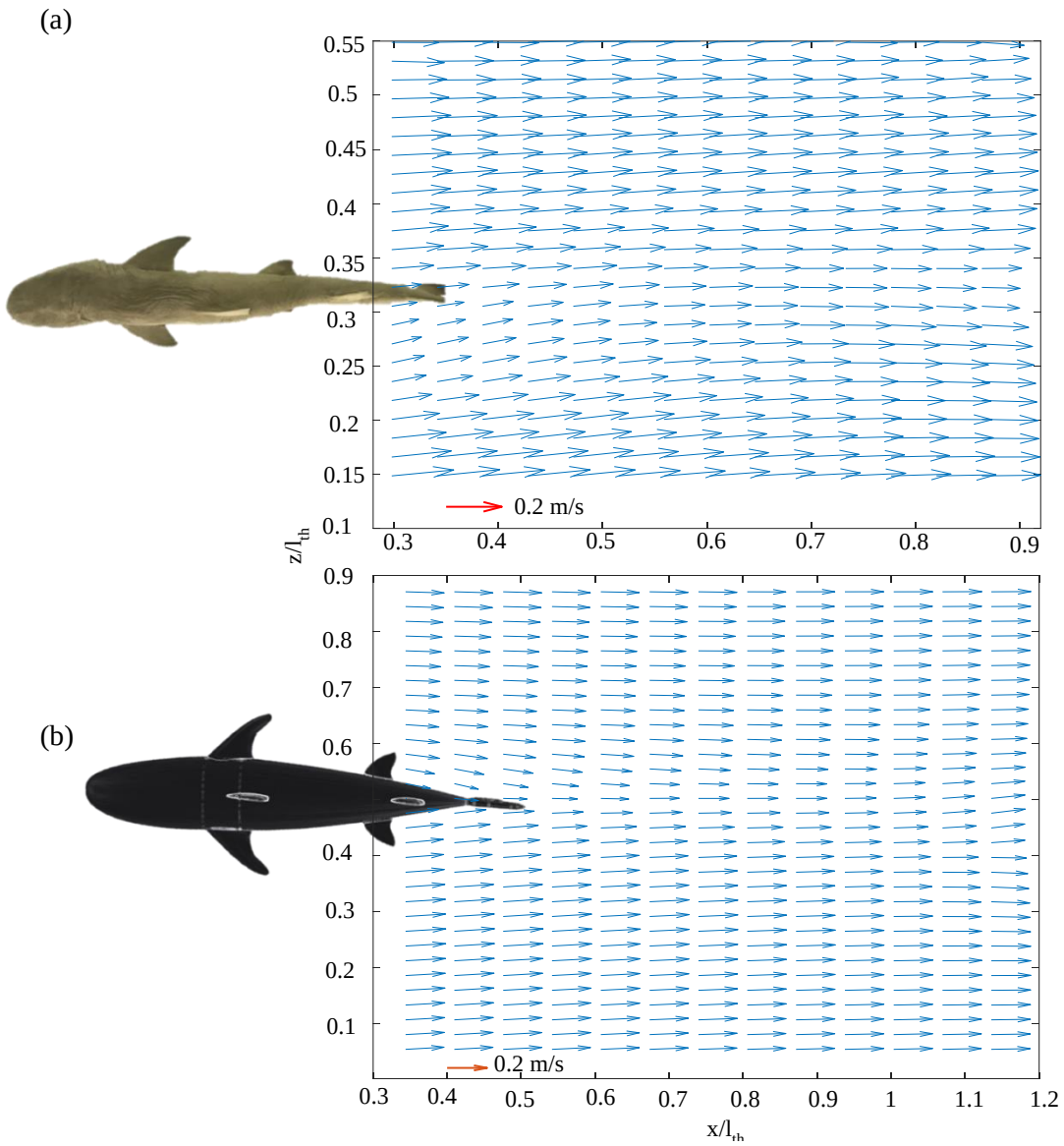

Figure 22: Mean velocity vector maps for LS-2DF (a) and LMS-2DF (b). The spanwise and streamwise positions are normalized by the maximum diameter of the body (l_{th}).

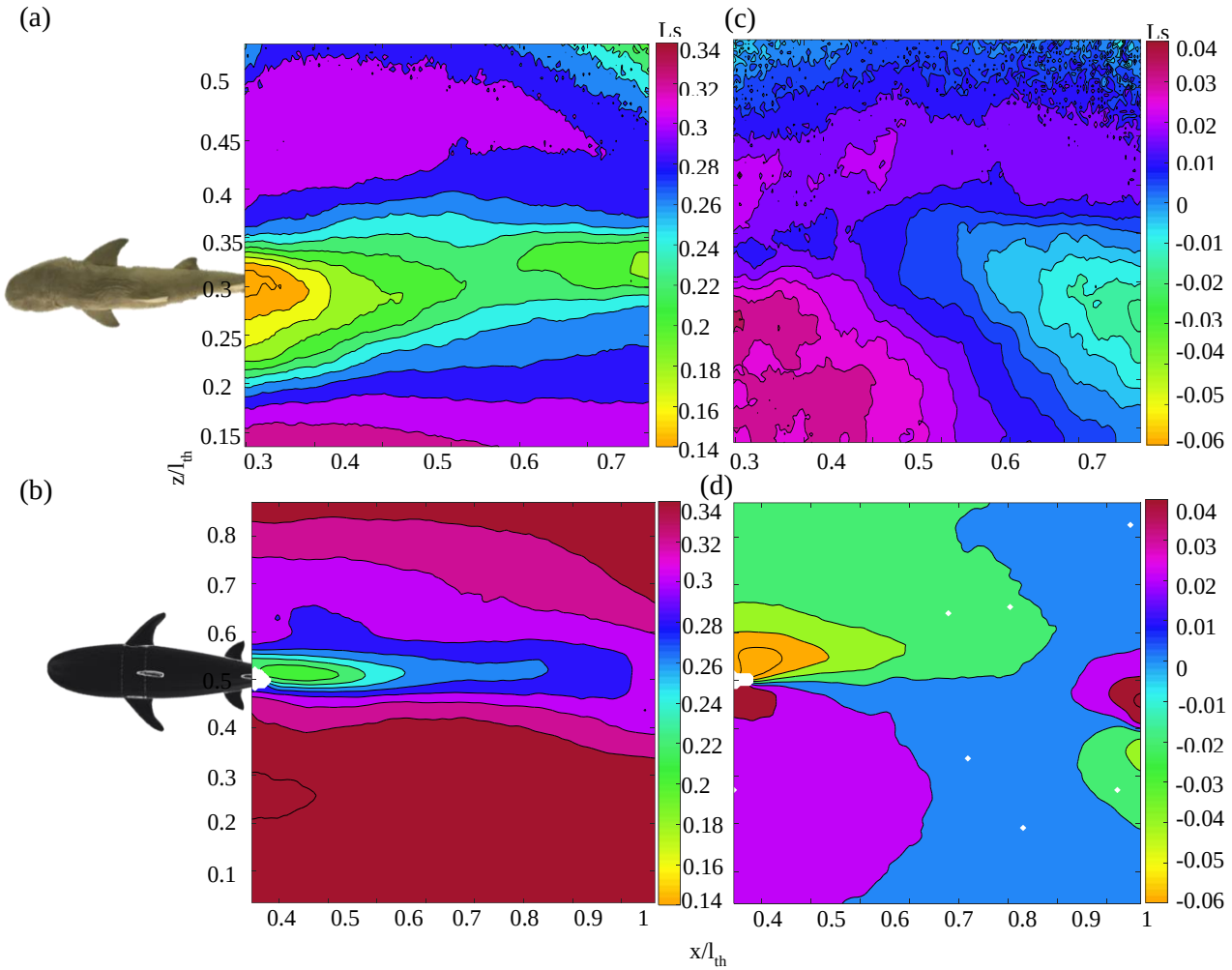

Figure 23: Mean velocity contours for streamwise velocity (a,b) and spanwise velocity (c,d) directions for LS-2DF (a,c), and LMS-2DF (b,d).

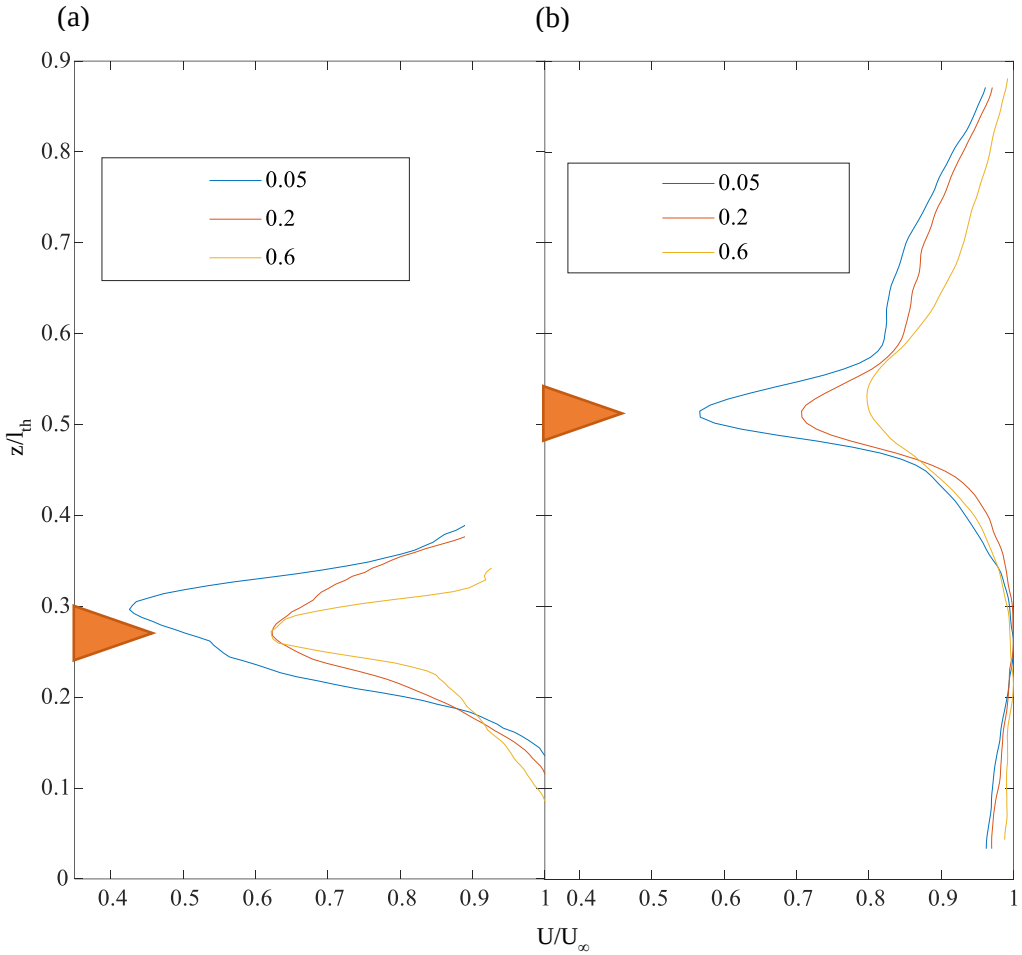

Figure 24: Mean streamwise velocity spanwise profiles for LS-2DF (a) and LMS-2DF (b) at various normalized downstream positions (see legend). An orange triangle marks where the tip of the fin is located.

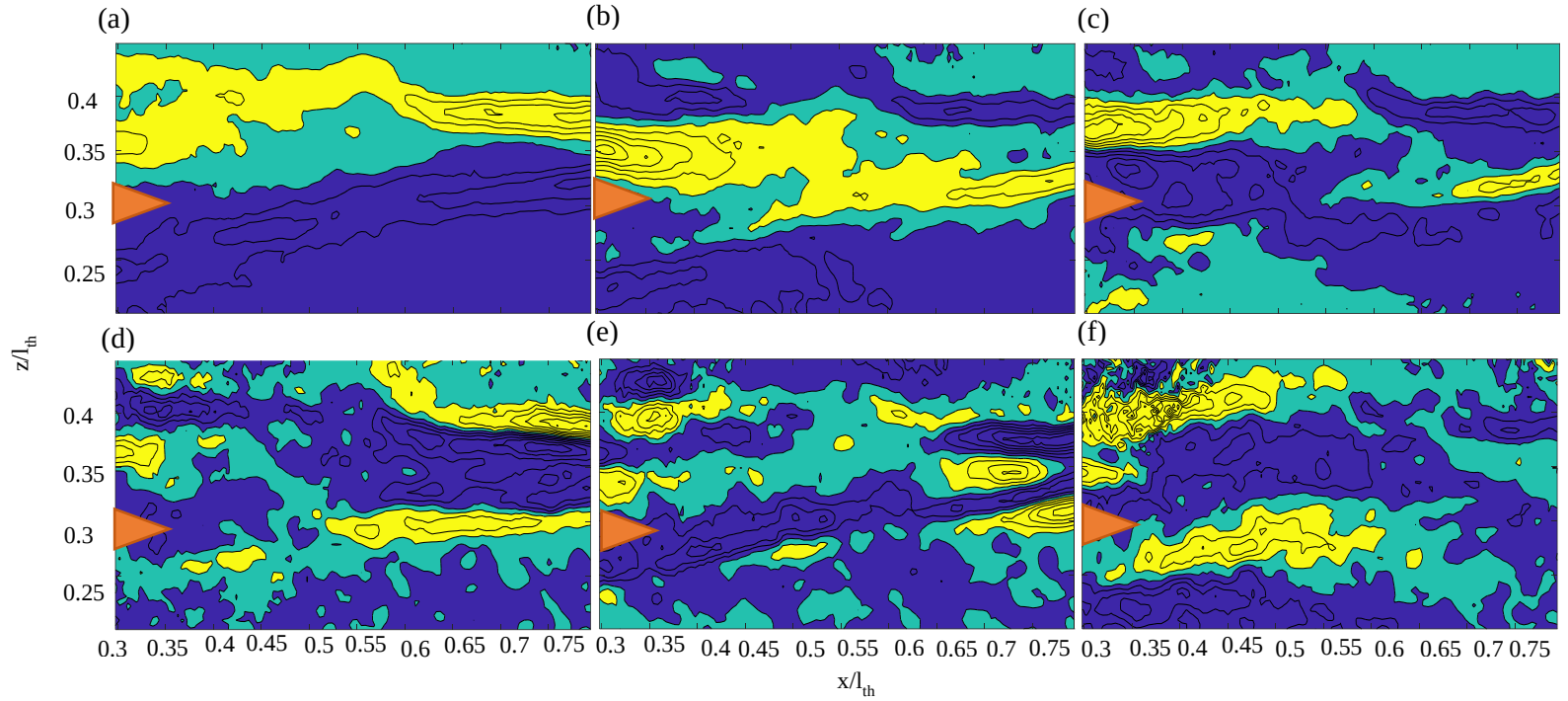

Figure 25: POD modes 1-6 (a-f, respectively) for LS-2DF. An orange triangle marks where the tip of the fin is located.

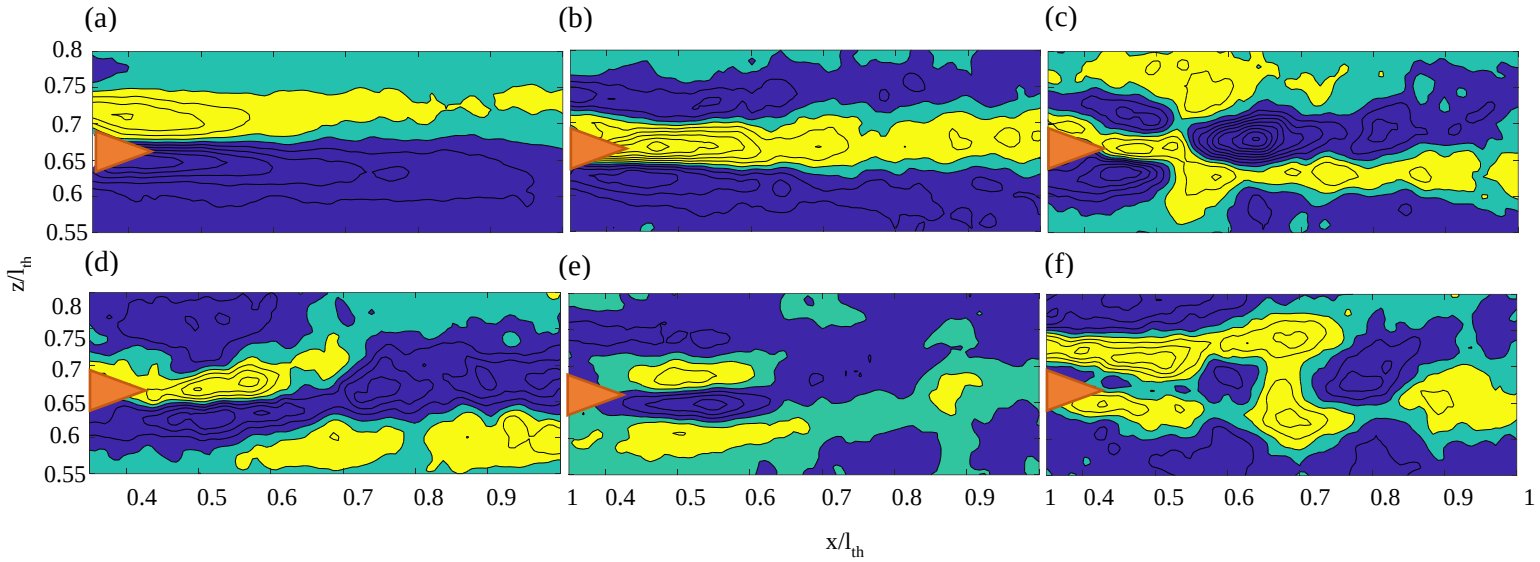

Figure 26: POD modes 1-6 (a-f, respectively) for LMS-2DF. An orange triangle marks where the tip of the fin is located.

5.2.2 *Hydrodynamic Forces*

The streamwise momentum spanwise deficit for the second dorsal fin of the Lemon Shark (LS-2DF and LMS-2DF) is shown in Figure 27. Both LS-2DF and LMS-2DF have similar deficit maxima at ~$4.0\times10^{-3}m^2s^{-2}$, but when comparing spanwise widths of the deficit LMS-2DF is approximately double (Figure 27). However, the primary differences in the widths occur in a region where the deficits are small; therefore, drag coefficients are relatively similar at 8.0×10^{-3} and 7.0×10^{-3} for LS-2DF and LMS-2DF, respectively (Table 3). For the deceased and model Lemon Shark, C_D for the 2DF is about twice that of the 1DF (Table 3). This result is also consistent with the corresponding velocity profiles that showed a larger reduction in velocity behind the 2DF (Figures 24, 27). Literature is limited on C_D of aquatic animal appendages, but it was found a robotic oscillating pectoral fin shows C_D at a magnitude of 10^{-3}, which is similar to the presented experimental results (Bandyopadhyay et al., 2008). C_T for 2DF could only be estimated for LMS because a vortex street was not identified behind LS; but for LMS C_T decreases from the first dorsal fin to the second for the Lemon Shark, which is inverse to the increase of C_D between these fins. Based on these results, it appears that the second dorsal fin creates lower thrust than the first dorsal fin.

From the prior section, results show a clear vortex street in the wake behind the first dorsal fin, however, that street is no longer present when the flow reaches the second dorsal fin. The POD behind the second dorsal fin shows that more modes are needed for 90% energy, which implies a more complex flow regime. Also, no vortex street is present behind the second dorsal fin and there is a larger wake produced by the second dorsal fin that is not

fully recovered prior to reaching the caudal fin. The wake behind the second dorsal fin also produces more drag than the first despite the similar size. These results strongly suggest that the presence of this large second dorsal fin interacts with the upstream flow from the peduncle region, as the distance between the second dorsal fin and leading edge of the caudal fin is small. Therefore, it's possible the wake of the second dorsal fin has an influence on the wake behind the body of the Lemon Shark.

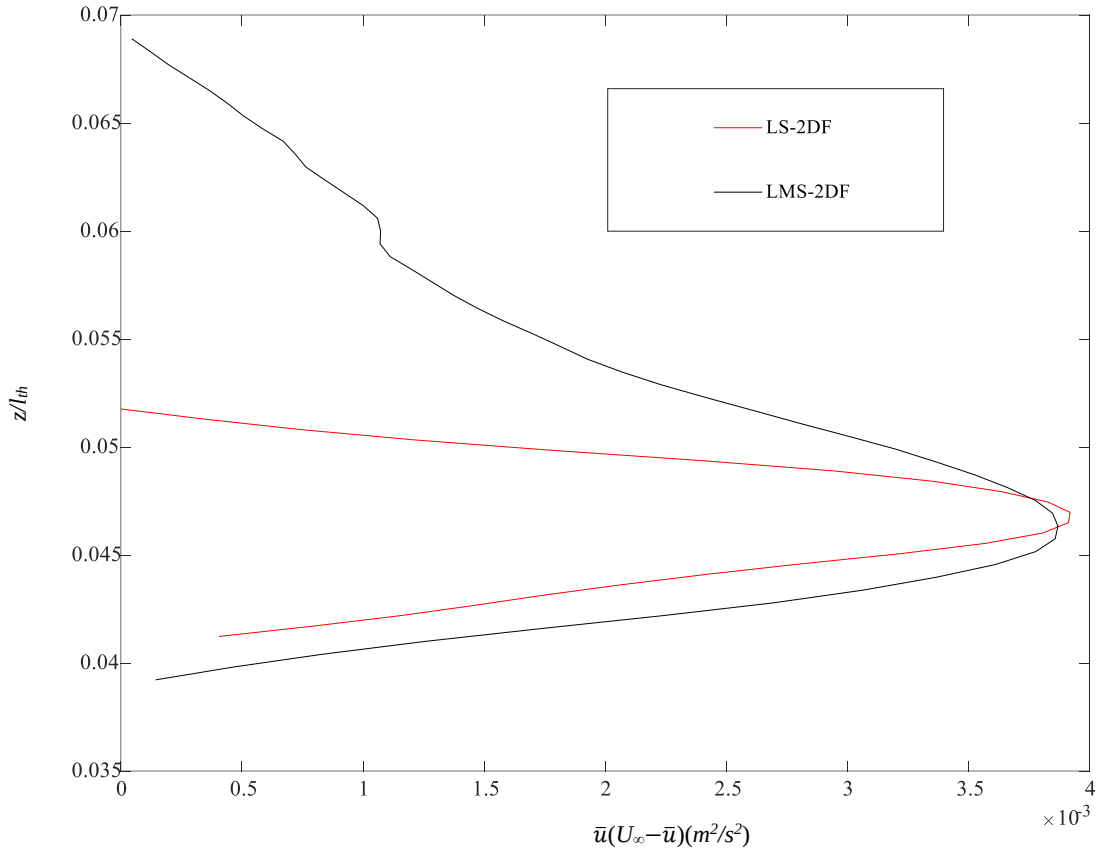

Figure 27: Mean streamwise momentum deficit vs. non dimensional spanwise distance for LS-2D and LMS-2DF (see legend).

5.3 Caudal Fin

5.3.1 Wake Characteristics

As stated in Section 5.1.1, mean velocity vector maps present an unclear visualization of the wake, which is also true for the wake behind the body shown in Figure 28. Mean velocity contour maps for *u* and *w* are shown in Figure 29 for the wake behind each specimen. These contour maps show a velocity deficit and recovery of the flow for *u* for all three configurations (Figure 29.a-c). As the downstream distance increases from the caudal fin, the velocity increases. It is important to note the wake does not fully recover to the freestream velocity within the FOV, but the flow is close to freestream velocities at a non-dimensional distance of ~1. SS-C presents the smallest change in *u*, with streamwise velocities at $0.14Ls^{-1}$ (Figure 29.a). LS-C and LMS-C present similar *u* contours with streamwise velocity minima at $\sim0.24Ls^{-1}$ (Figure 29.b, Figure 29.c). The dissimilarity in *u* velocities for the wake behind the body of the Spinner Shark and Lemon Shark are the result of differences in L_T of the sharks, as the deceased Spinner Shark is roughly 30cm longer than the deceased Lemon Shark.

It was reported that live semi-captive juvenile Lemon Sharks show swimming speeds between 0.2 and $0.4Ls^{-1}$ (Bouyoucos et al., 2017) similar to the setup here, but there is currently no existing literature on swimming speeds of the Spinner Shark due to misidentification of the species (Branstetter, 1982). Despite limited information known of the Spinner Shark, the mean *u* for SS-C is much lower than what is expected from a live swimming shark of similar size which must swim at $20cms^{-1}$, or $0.28Ls^{-1}$, in order to ram

ventilate (Graham et al.,1990). This observation could suggest that the incoming flow speed should be faster in order to better replicate swimming speeds for the Spinner Shark.

The mean spanwise velocity, $\overline{w}$, is an order of magnitude slower than the streamwise velocity, with velocities on the order of 10^{-2} and 10^{-3} (Figure 29.d-f). For SS-C the flow reaches close to $0Ls^{-1}$ directly behind the caudal fin (Figure 29.d). LS-C mean $\overline{w}$ contour shows faster *w* that decreases at increasing *z* in the spanwise direction (Figure 29.e). LMS-C shows a decrease in $\overline{w}$ velocity at increasing *z* in the spanwise plane, and approaches close to zero behind the caudal fin (Figure 29.f).

Mean streamwise velocity spanwise profiles at various x/l_{th} positions are shown in Figure 30. The largest deficit width is for SS-C: covering a non-dimensional distance of ~0.45 (almost half of l_{th},) with a ~30% decrease in flow from the freestream (Figure 30.a). LS-C has a slightly smaller wake, covering a non-dimensional distance of 0.4 and a ~20% decrease in flow from the freestream (Figure 30.b). LMS-C also has a wake that extends to roughly 0.4 of l_{th} in width and ~25% decrease in flow from the freestream, which is a slightly larger decrease in flow than LS-C (Figure 30.c). SS-C and LS-C show a similar recovery in respect to the distance from the caudal fin based on the maximum diameter of the body (Figure 30.a, Figure 30.b). These results suggest that the wake is close to recovery when the flow reaches a distance equal to the maximum diameter of the body. However, it is unclear if the wake for LMS-C fully recovers at this distance, as a distance equal to the maximum diameter of the body cannot be seen within the FOV (Figure 30.c).

The cumulative relative energy of the modes, which represents the total entropy in the control volume (i.e., the PIV FOV) versus the number of modes for SS-C, LS-C, and LMS-C is shown in Figure 16. LMS-C requires 160 modes to represent 90% of the variance of

the vorticity, whereas SS-C required 105 modes, and LS-C required 75 modes. SS-C (Figure 31.a, Figure 32) shows evidence of a vortex street in modes 3 and 5, LS-C (Figure 31.b, Figure 33) in modes 3, 4, and 6, and LMS-C (Figure 31.c, Figure 34) in mode 5. It is important to note that there is at most ~10% difference in relative energy between mode 3 and mode 5 for all specimens; therefore, results are considered comparable.

From the street present in the dominant modes, the spacing ratio and stability criteria can be computed. Results show spacing ratio values for the Lemon Shark (LS-C and LMS-C) meet the von-Karman stability criteria of the wake, with a spacing ratio close to 0.28 as shown in Table 4. Using the spacing ratio to estimate Strouhal number (Eqn. 5), it was found that *St* numbers are consistent for LS-C and LMS-C, and both fall within the expected 0.2-0.4 range for swimming organisms (Eloy, 2012; Taylor et al., 2003) (Table 4). Figure 35 shows the Strouhal numbers for this study along with those of other studies versus *Re* (Wu, 1971; Webb and Kostecki, 1984; Fish et al., 1988; Fish, 1998; Eloy, 2012). Compared to the existing literature, the Lemon Shark features a similar *St* number as the Scallop Hammerhead Shark (Eloy, 2012). These results provide evidence that the Lemon Shark is at the peak of its propulsive efficiency as stated by Taylor (2003). In contrast, the Spinner Shark appears less efficient and the spacing ratio does not meet the von-Karman stability criteria. However, this could be the result of an incorrect flow velocity (or swimming speed) for this species because the flow speed in the flume was set to match that of a Lemon Shark swimming in-vivo. These results also suggest that when the von-Karman stability criteria is met, the *St* number is within the 0.2-0.4 range.

Table 4: Wake characteristics based on POD analysis applied to the vorticity field; vortex wavelength, a, cross stream distance, b, spacing ratio, $\frac{b}{a}$, and Strouhal number, St for each caudal fin configuration.

Experiment	a (m)	b (m)	b/a	St
SS-C	0.040	0.005	0.12	0.13
LS-C	0.026	0.007	0.27	0.37
LMS-C	0.020	0.006	0.33	0.38

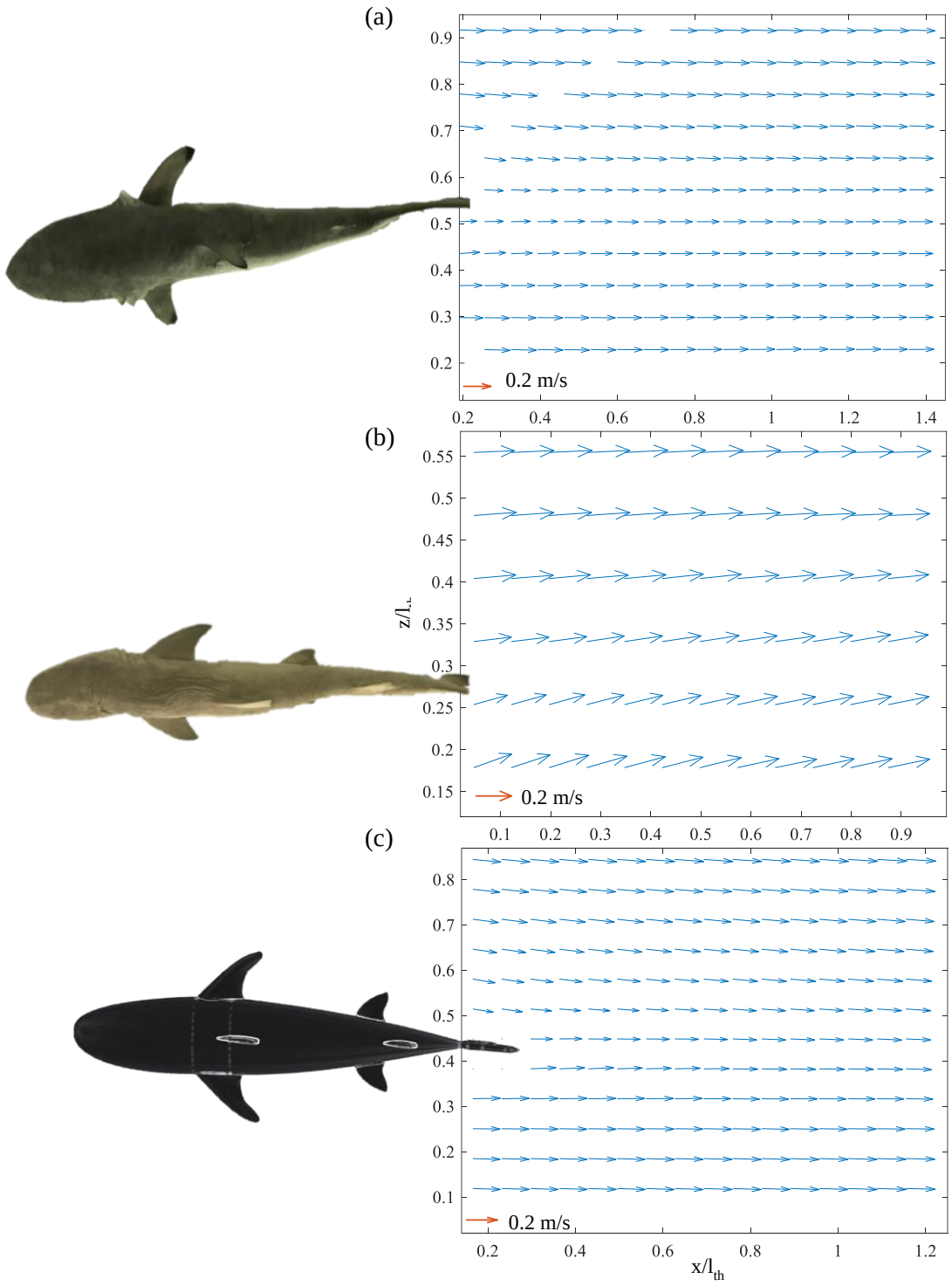

Figure 28: Mean velocity vector maps for SS-C (a), LS-C (b), and LMS-C (c). The streamwise and normal positions are normalized by the maximum diameter of the body (l_{th}).

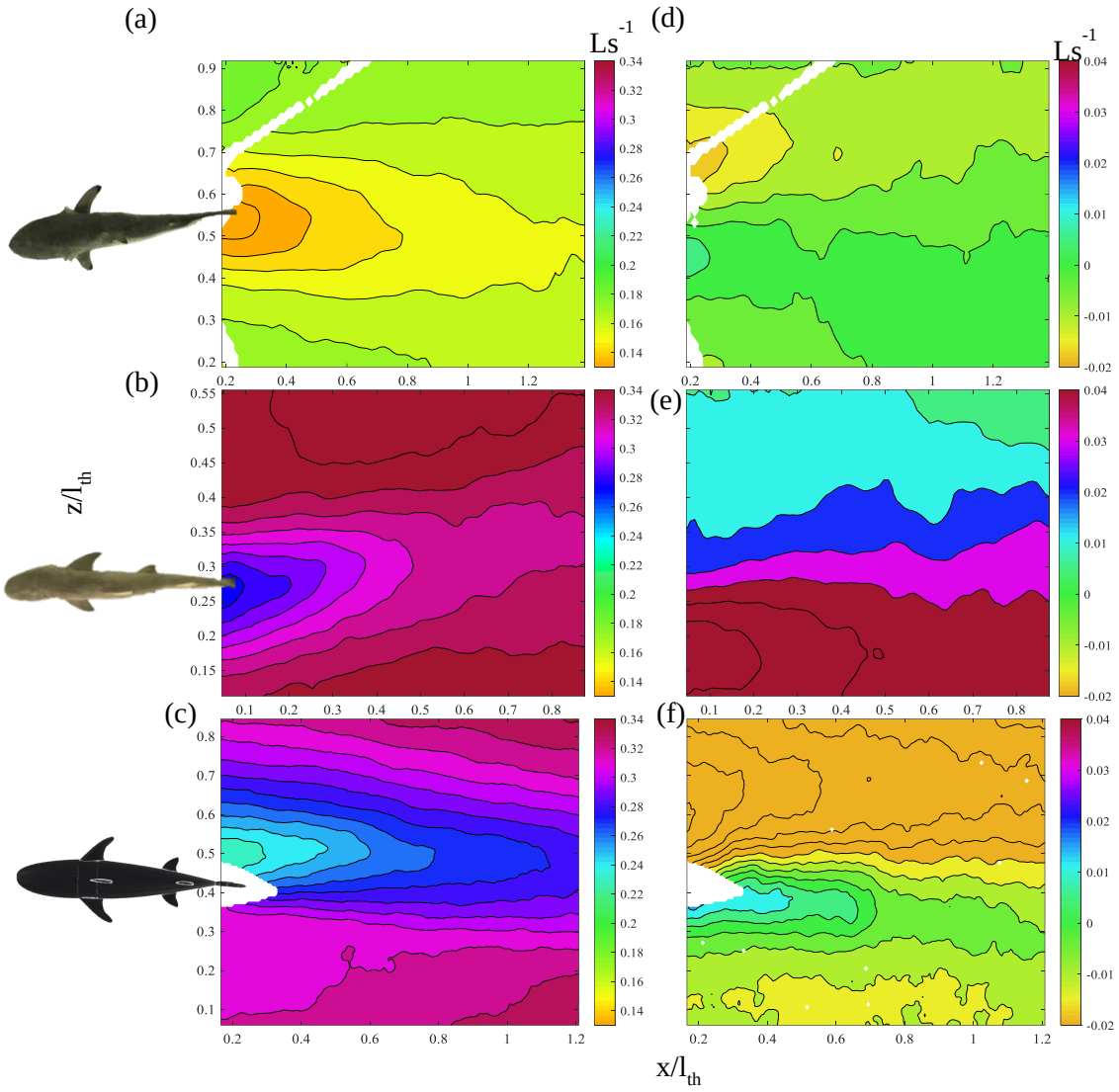

Figure 29: Mean velocity contours for *u* (a-c) and *w* (d-f) for SS-C (a,d), LS-C (b,e), and LMS-C (c,f).

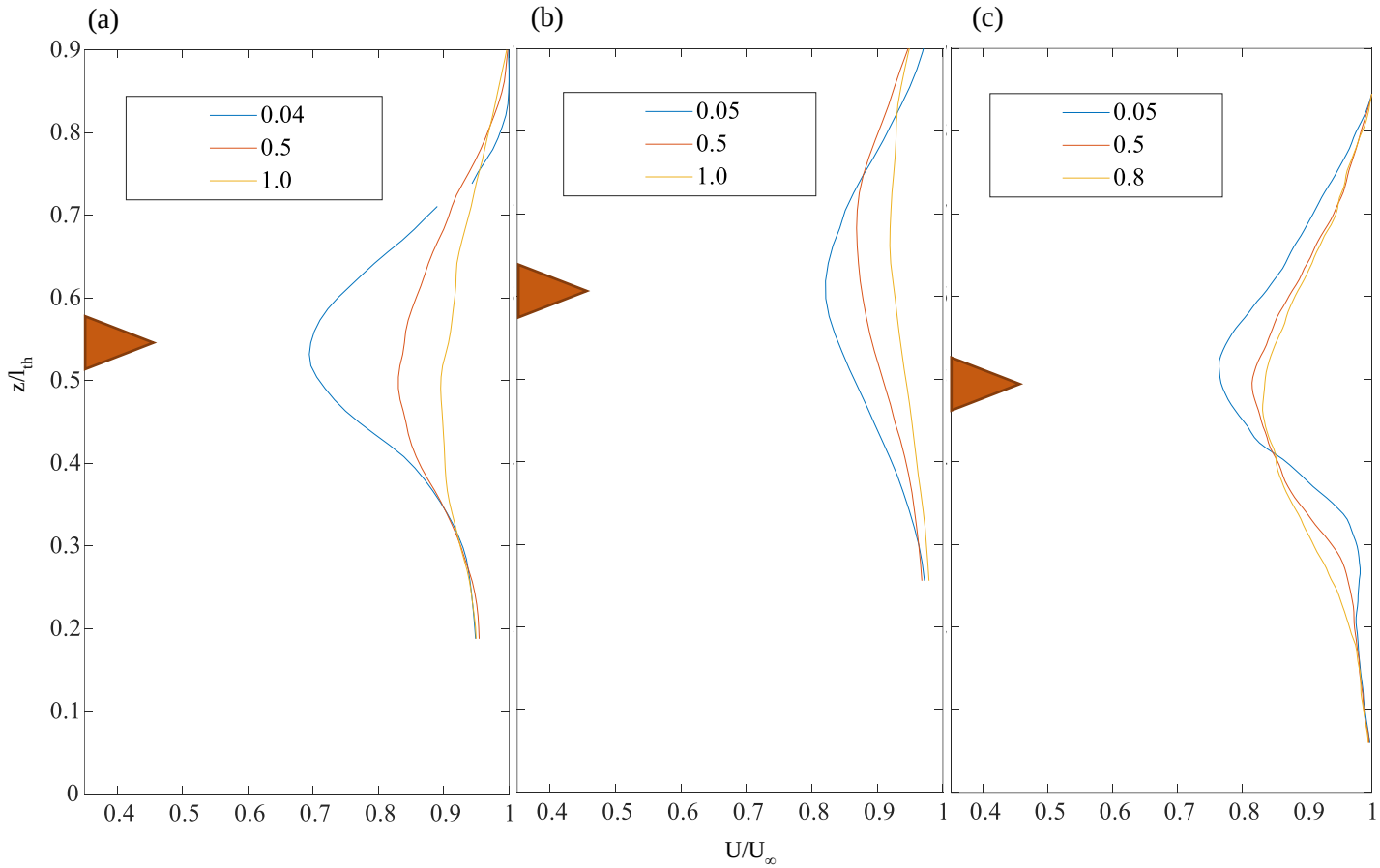

Figure 30: Mean streamwise velocity spanwise profiles for SS-C (a), LS-C (b), and LMS-C (c) at various downstream positions (see legend). An orange triangle marks where the tip of the caudal fin is located

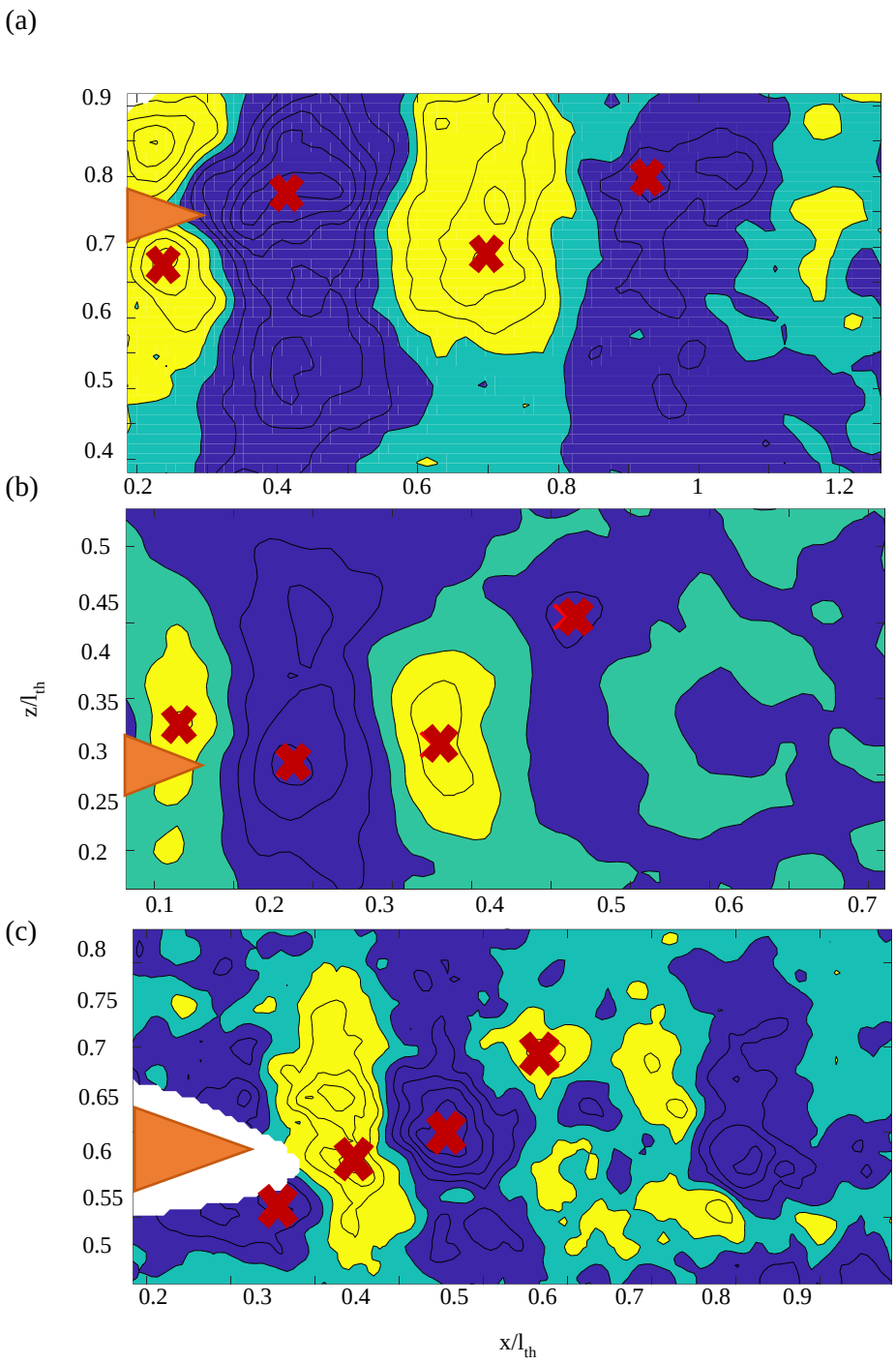

Figure 31: Lowest POD mode exhibiting a vortex street for SS-C (mode 3), LS-C (mode 3), and LMS-C (mode 5). The red "x" indicates the center of circulation for each vortex based on swirling strength. An orange triangle marks where the tip of the caudal fin is located.

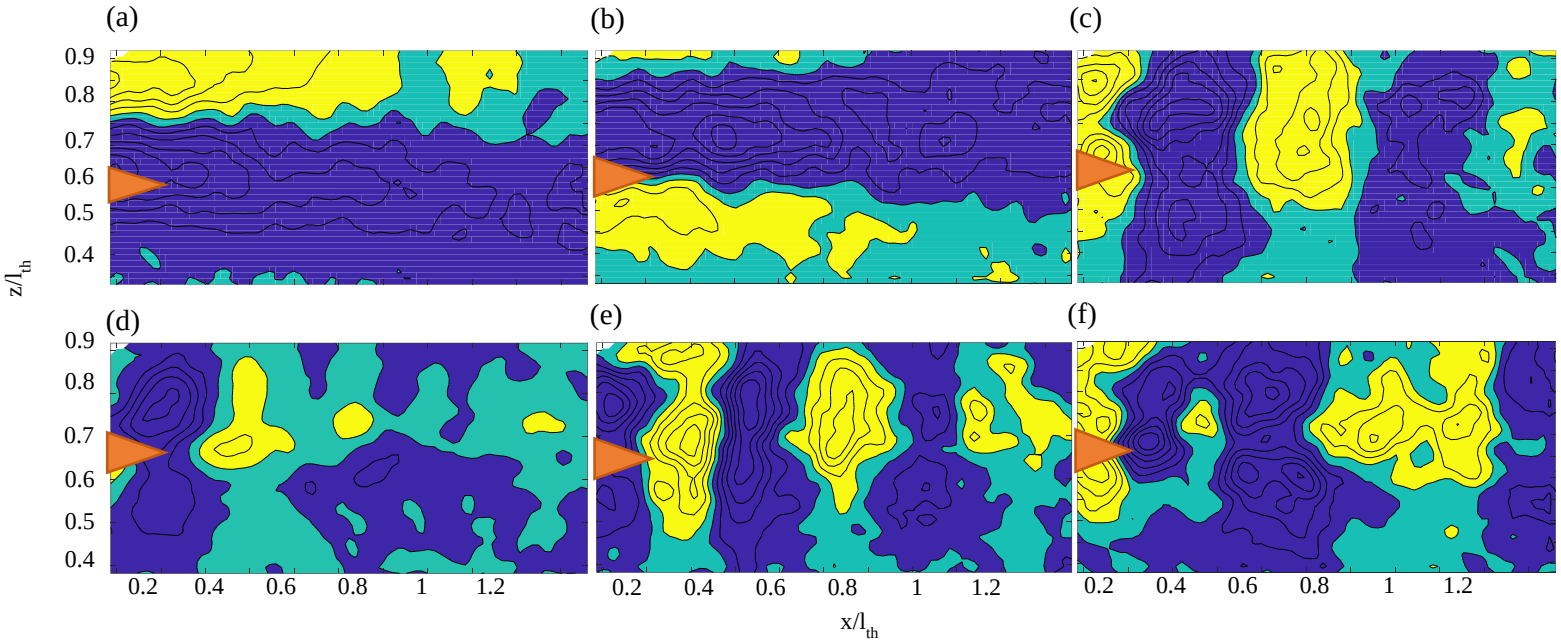

Figure 32: POD modes 1-6 (a-f, respectively) for SS-C. An orange triangle marks where the tip of the caudal fin is located.

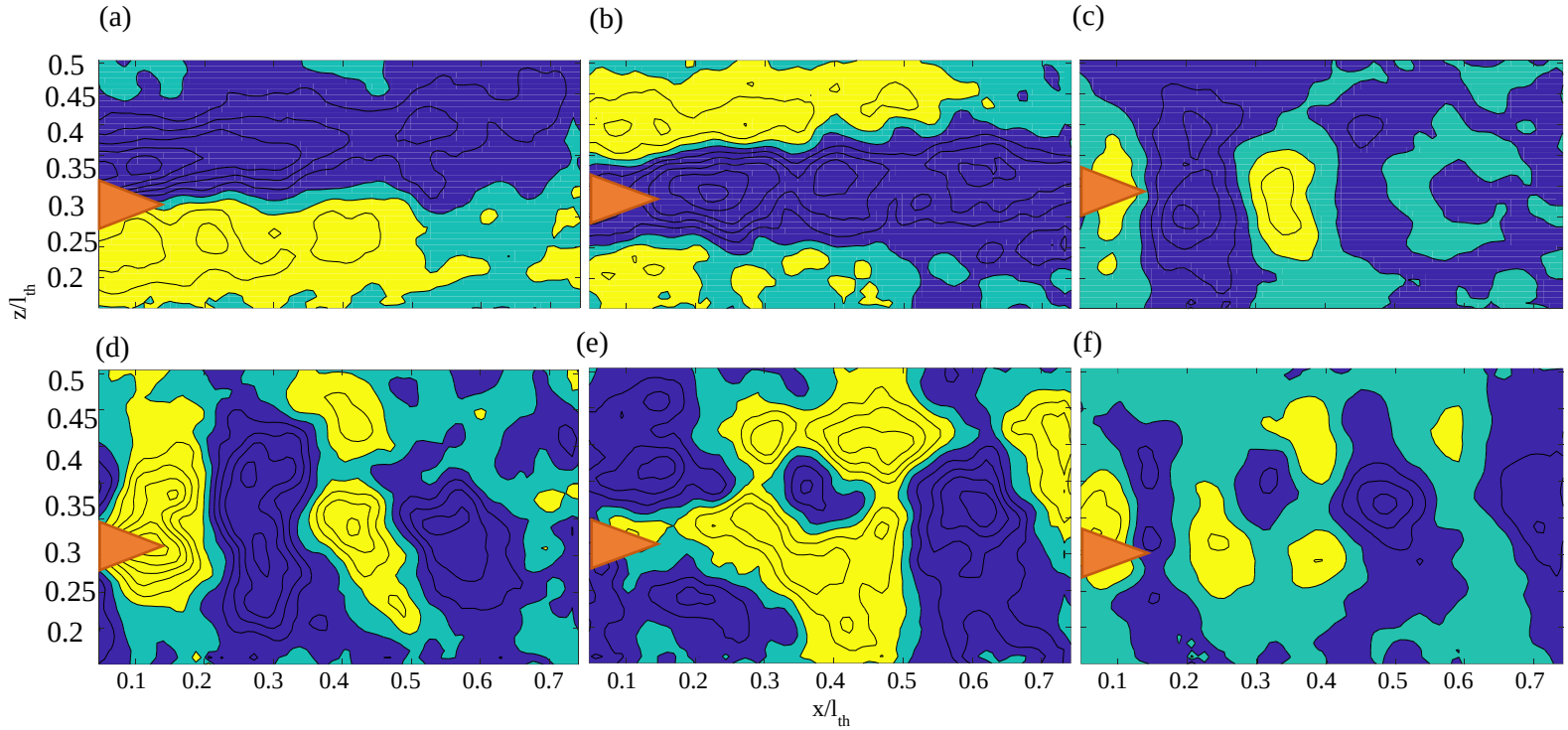

Figure 33: POD modes 1-6 (a-f, respectively) for LS-C. An orange triangle marks where the tip of the caudal fin is located.

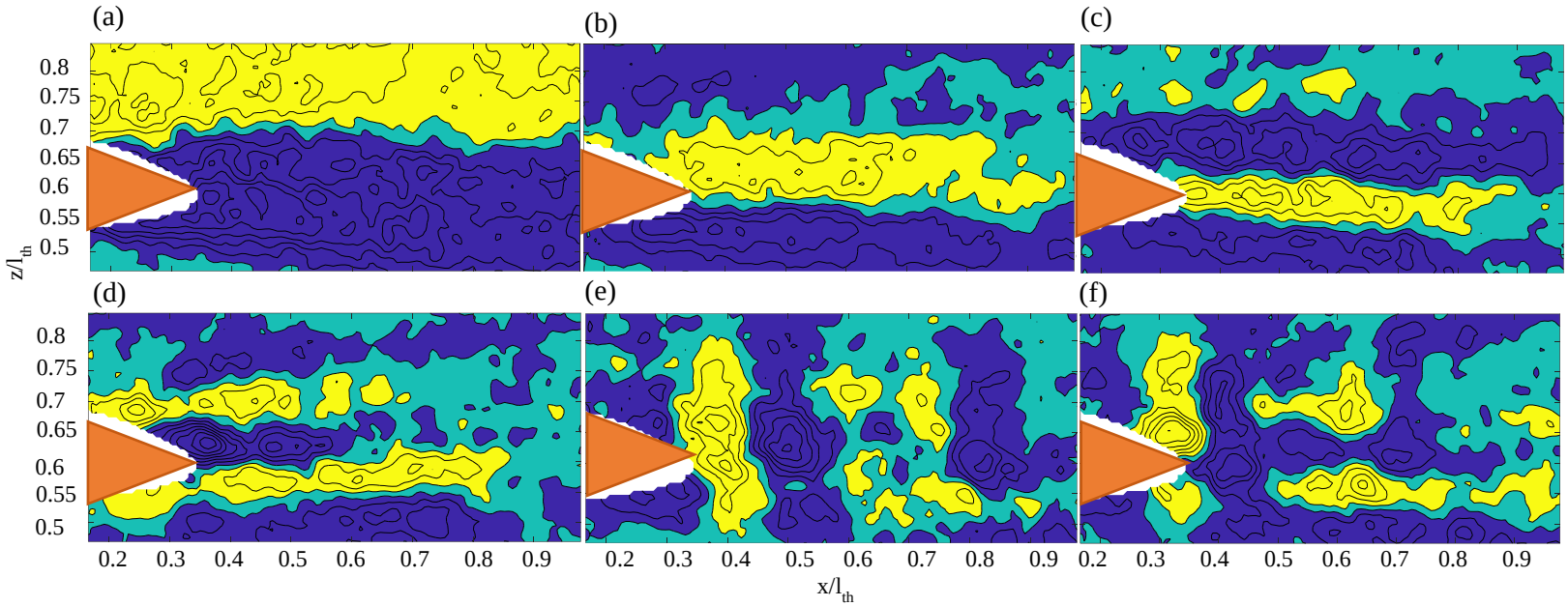

Figure 34: POD modes 1-6 (a-f, respectively) for LMS-C. The caudal fin is represented by orange triangle in each image.

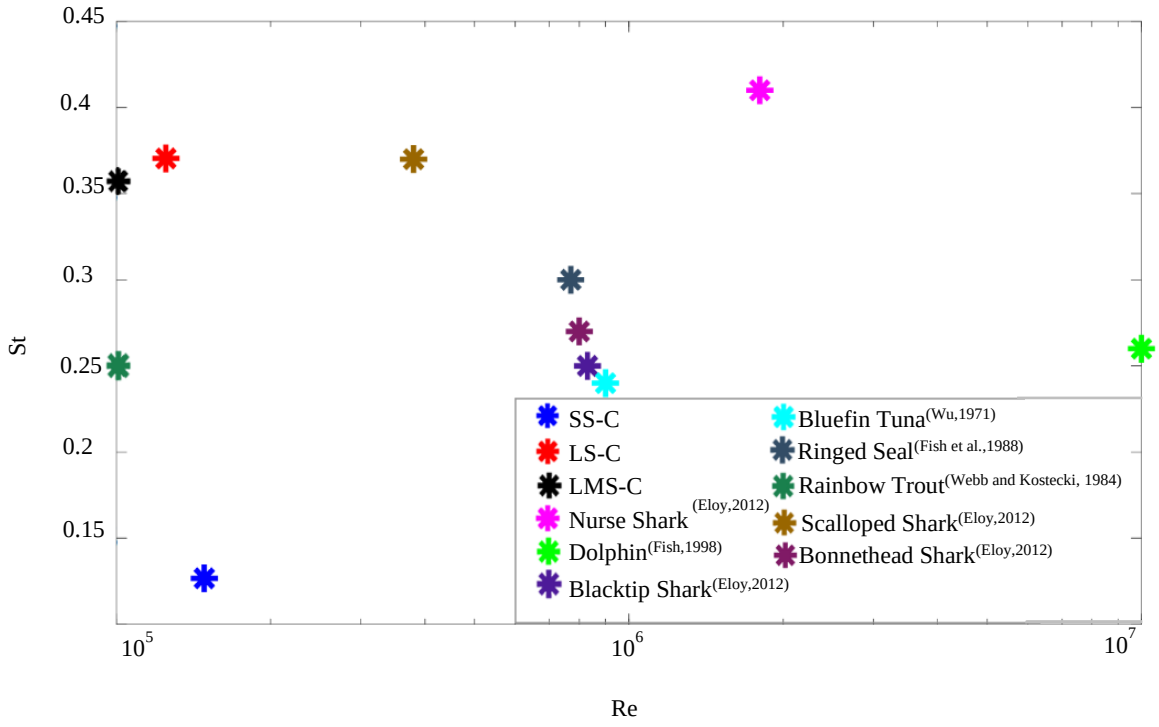

Figure 35: Reynolds number vs. Strouhal number for experiments and literature.

5.3.2 Hydrodynamic Forces

Mean streamwise momentum spanwise deficits used to compute the drag force for SS-C, LS-C, and LM-C are shown in Figure 36. All three configurations present a spanwise momentum deficit width approximately equal to the maximum diameter of the body (Figure 36). Table 3 shows the resulting drag coefficients where the Spinner Shark has a larger drag coefficient. LS-C has the smallest C_D, 0.01 (Table 3). When comparing C_D of these experiments to the literature shown in Figure 37, the LS-C C_D is similar to that of the Bluefin Tuna and Sailfish (Wu, 1971; Alexander, 1990), which are considered to be highly efficient, fast swimmers. LMS-C has a slightly higher C_D at 0.02 and is most similar to the Rainbow Trout (Webb, 1971; Webb and Kostecki, 1984). SS-C has the highest C_D, 0.03, which is most like that of the Harp Seal (Fish et al., 1988). Overall, the Spinner Shark has larger drag compared to the Lemon Shark. This result strongly suggests that the wake behind the second dorsal fin interacts with the upstream flow produced by the leading edge of the caudal fin, which prevents formation of a new vortex street behind the second dorsal fin, enabling more uniform flow at the caudal fin; thus, reducing the size of the overall wake behind the shark and ultimately reducing the drag. This speculation is consistent with the observation that the drag based on measurements behind the caudal fin of the Lemon Shark is lower than that of the Spinner Shark, which does not possess this second dorsal fin.

Other research has found that the drag coefficient of a cylinder can be reduced by the placement of a smaller cylinder upstream (Imron, et al., 2017). This effect is the result of a narrowing of the velocity profile due to the presence of the smaller upstream cylinder. It was also found that if the placement of the smaller cylinder is closer to the larger cylinder, then the drag coefficient is reduced more so than having the small cylinder placed farther

upstream (Imron, et al., 2017). This supports the idea that the second dorsal fin could contribute to a reduction in drag based on the overall wake behind the body, as the placement of the second dorsal fin is close to the caudal fin.

Thrust coefficient results in Table 3 show a higher coefficient for the Lemon Shark than the Spinner Shark. Although independent estimates of the drag coefficient and thrust coefficient were made, they both yield results that are within a factor of two. The coefficient of thrust and drag for SS-C was 0.04 and 0.03 respectively, indicating equilibrium of the two forces, while for LS-C and LMS-C there was a slightly larger difference. Despite these differences, it appears that estimating C_T using Eqn. 12 as initially suggested by Bearman (1967) yields accurate results of the thrust acting on the body of a shark.

Figure 38 shows the vortex spacing ratio versus C_T for LS-C, LMS-C, and SS-C. The Kronauer stability criteria, Eqn. 8 (Section 4.5), is reflected by the slope between two points in this figure. The figure shows a slope of nearly zero for both the Lemon Shark and the Spinner Shark, which satisfies the stability criterion in Eqn. 8 (Figure 38), indicating that C_T doesn't vary with respect to variations b/a. Therefore, we can assume that the street is stable for all three configurations. Collectively, these results suggest that the Lemon Shark produces a higher thrust and lower drag than the Spinner Shark.

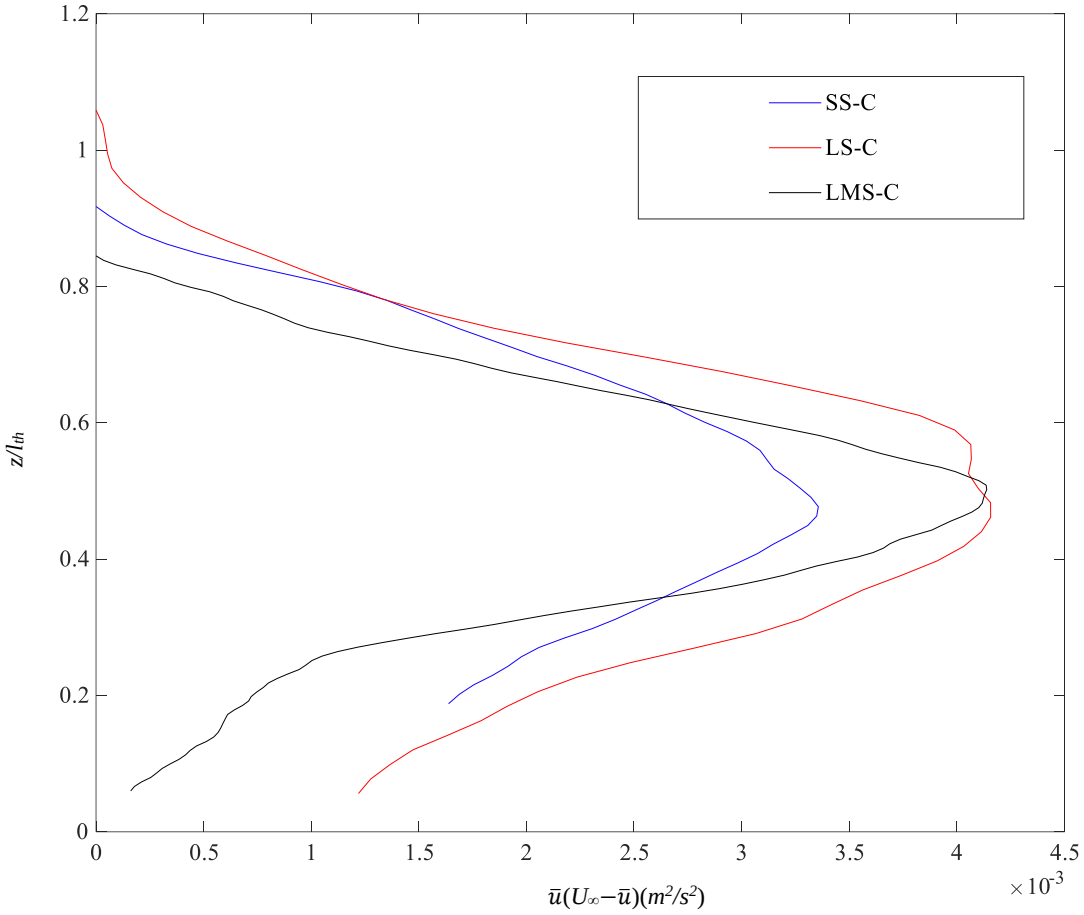

Figure 36: Mean streamwise momentum deficit vs. non dimensional spanwise distance for SS-C, LS-C, and LMS-C (see legend).

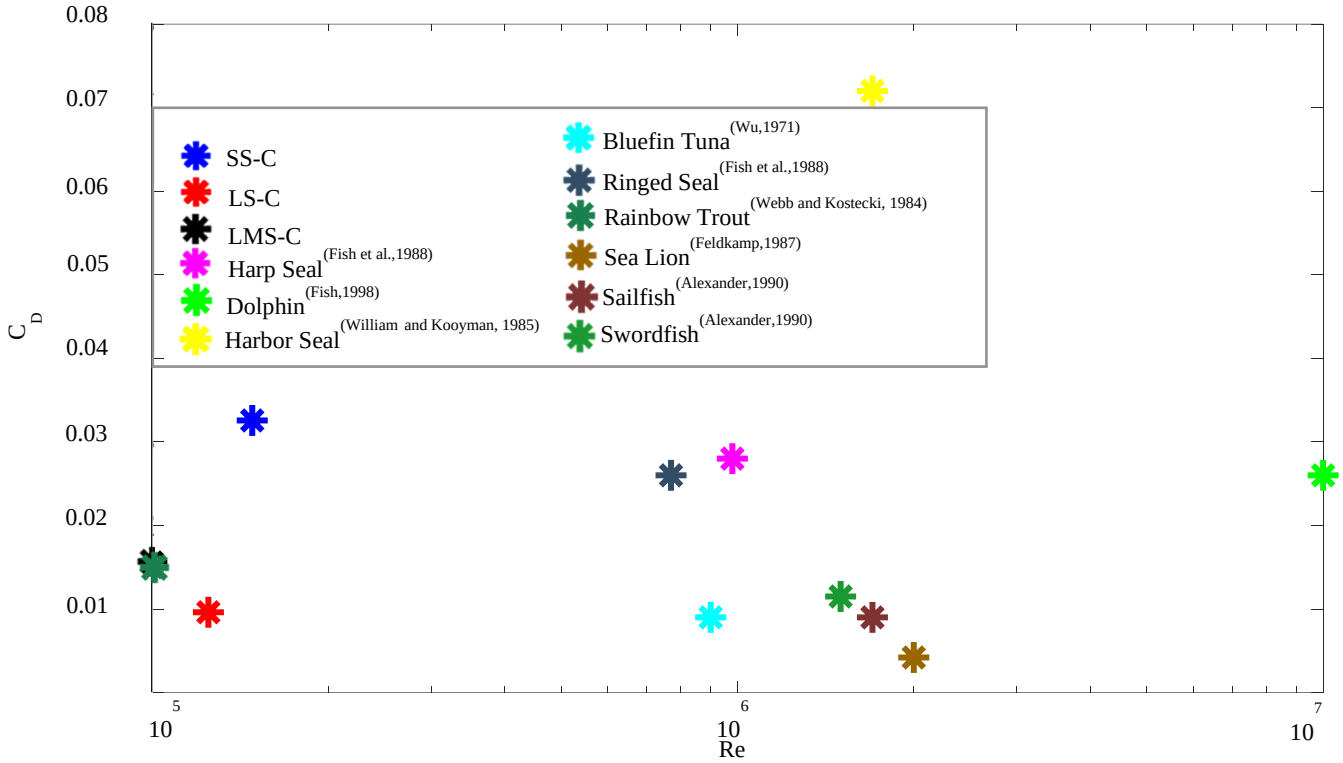

Figure 37: Reynolds number vs. drag coefficients from experiments and literature (see legend).

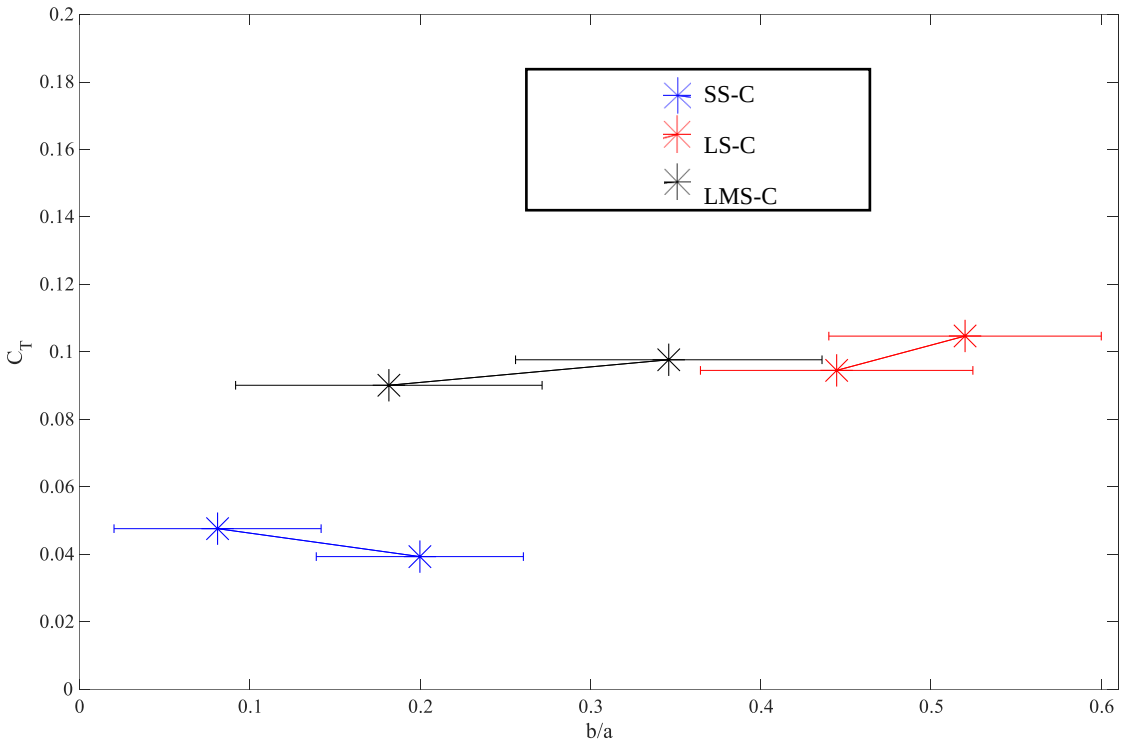

Figure 38: Vortex spacing ratio (*b*/*a*) vs. thrust coefficient (C_T) for caudal fin configurations. Error bars show standard deviation from the mean spacing ratio.

6.0 Summary and Conclusions

Understanding the hydrodynamic function of a shark's morphological features, like median fin function, can benefit advancements in technology, such as addressing efficiency issues in AUVs. The purpose of this study is to better understand morphological features in sharks, specifically the second dorsal fin of the Lemon Shark. In order to improve our understanding of the hydrodynamic role of the second dorsal fin of the Lemon Shark, we: i) evaluated the wake characteristics behind a deceased and model Lemon Shark with two large dorsal fins and compared these characteristics to those of a deceased Spinner Shark with one large dorsal fin and ii) examined what effect these characteristics have on the hydrodynamic forces (thrust and drag) acting on the sharks. These objectives were studied through eight experiments that used a non-intrusive flow imaging technique (PIV) to measure the wake behind the first dorsal fin, second dorsal fin, and caudal fin for the two different species of shark in the spanwise-streamwise plane.

A POD applied on vorticity fields in the wake (obtained from PIV measurements) was used to characterize and quantify the vortex street formed within the wake. The vortex spacing ratio and a non-traditional Strouhal number were computed from the wake characteristics, and the stability of the street was evaluated using von-Karman and Krouner stability criterions. The hydrodynamic forces thrust, and drag were estimated using the spacing ratio and the momentum deficit in the wake, respectively.

Results characterizing the flow behind the dorsal fins and caudal fin provide evidence that the Lemon Shark's second dorsal fin interacts with the flow upstream of the caudal fin

thereby influencing drag during steady swimming. Wake characteristics behind the first dorsal fin of the Lemon Shark present a stable vortex street. Due to the distance between the first and second dorsal fin of the Lemon Shark the street shed from the first dorsal fin does not affect the flow immediately upstream to the second dorsal fin. The second dorsal fin has a larger velocity deficit than the first dorsal fin despite being similar in size, which yields larger drag behind the second dorsal fin compared to the first dorsal fin. There is also no vortex street present in the wake behind the second dorsal fin, which could be the result of flow interaction between the second dorsal fin and the caudal fin that prevents the street from forming. This interaction between the second dorsal fin and caudal fin is due to the distance between the two fins being relatively short, and results in a reduction in size of the overall wake behind the shark. The reduction in size of the wake behind the shark ultimately results in a lower drag on the Lemon Shark compared to the Spinner Shark (a species with only one large dorsal fin). Consistent with these findings the Lemon Shark exhibits a *St* that falls within the ideal range for optimal swimming efficiency, while the Spinner Shark does not.

We also found that Bearman's (1967) method (Eqn.12) to compute the coefficient of thrust based on the wake characteristics can serve as an accurate representation of thrust, as results are generally consistent with those computed from a traditional drag estimate (Goett, 1939; Eqn.10). In summary, we suggest that the second dorsal fin plays a role in the overall wake of the Lemon Shark by interaction with the caudal fin upstream flow that reduces the overall size of the wake behind the body and reduces the drag. Future research

should include undulation of the shark, using a model or living organisms, to examine how the undulation interacts with these morphological features and whether similar results are found when undulation is included.

7.0 *Works Cited*

Adrian, R.J. 1991. Particle-imaging techniques for experimental fluid mechanics. Annual review of fluid mechanics, 23: 261-304.

Adrian, R.J. 1997. Dynamic ranges of velocity and spatial resolution of particle image velocimetry. Measurement science and technology, 8: 1393-1398.

Adrian, R.J., Westerweel, J. 2011. Particle image velocimetry. Cambridge University Press.

Affleck, R.J. 1950. Some points in the function, development and evolution of the tail in fishes. Proceedings of the zoological society of London, 120: 349–368.

Alexander, D.E. 1990. Drag coefficients of swimming animals: Effects of using different reference areas. Biological bulletin, 179: 186-190.

Alexander, R.M. 1965. The lift produced by the heterocercal tails of selachii. Journal of experimental biology, 43: 131–138.

Afroz, F., Lang, A., Habegger, M.L., Motta, P., Hueter, R. 2016. Experimental study of laminar and turbulent boundary layer separation control of shark skin. Bioinspiration and biomimetics, 12: 1-18.

Anderson, J.D. 1989. Introduction to flight 3rd edition. New York, New York. McGraw-Hill.

Anderson, J.D. 2011. Fundamentals of Aerodynamics. New York, New York. McGraw-Hill.

Bandyopadhyay, P.R., Beal, D.N., Menozzi, A. 2008. Biorobotic insights into how animals swim. Journal of experimental biology, 211: 206-214.

Bass, A.J., D'Abrey, J.D., Kistnasamy, N.1975. Sharks of the east coast of southern Africa. IV. The families *Odontaspididae, Scapanorhynchidae, Isuridae, Cetorhinidae, Alopiidae, Orectolobidae,* and *Rhiniodontidae*. Oceanographic research institute.

Bearman, P.W. 1967. On vortex street wakes. Journal of fluid mechanics, 28(4): 625-641.

Ben-Gida, H., Kirchhefer, A., Taylor, Z.J., Bezner-Kerr, W., Guglielmo, C.G., Kopp, G.A., Gurka, R. 2013. Estimation of unsteady aerodynamics in the wake of a freely flying European starling (*Sturnus vulgaris*). PLoS ONE, 8(11): e80086.

Berkooz, G., Holmes, P., Lumley, J.L. 1993. The proper orthogonal decomposition in the analysis of turbulent flows. Annual review of fluid mechanics, 25:539-575.

Bone, Q. 1978. Locomotor muscle. Fish Physiology, 7: 361–424. Academic Press, New York.

Bouyoucos, I.A., Montgomery, D.W., Brownscombe, J.W., Cooke, S.J., Suski, C.D., Mandelman, J.W., Brooks, E.J. 2017. Swimming speeds and metabolic rates of semi-captive juvenile Lemon sharks (*Negaprion brevirostris*, Poey) estimated with acceleration biologgers. Journal of experimental biology and ecology, 486: 245-254.

Branstetter, S. 1987. Age and growth estimates for Blacktip, *Charcharhinus limbatus*, and Spinner, *C. brevipinna*, sharks from the northwestern Gulf of Mexico. Copeia, 4:964-974.

Brett, J.R., and Blackburn, J.M. 1978. Metabolic rate and energy expendiure of the Spiny Dogfish, *Squalus acanthias.* Journal of the fisheries research board of Canada, 35:816-821.

Brewster, L.R., Dale, J.J., Guttridge, T.L., Gruber, S.H., Hansell, A.C., Elliott, M., Cowx, I.G., Whitney, N.M., Gleiss, A.C. 2018. Development and application of a machine learning algorithm for classification of elasmobranch behavior from accelerometry data. Marine biology, 165(4): 62.

Brooks, S.A., Green, M.A. 2019. Experimental study of body-fin interaction and vortex dynamics generated by a two degree-of-freedom fish model. Biomimetics, 4(67): 1-23.

Brown, C.A., Gruber, S.H. 1988. Age assessment of the Lemon shark, *Negaprion brevirostris* using tetracycline validated vertebral centra. Copeia, 1988(3): 747-753.

Bushnell, D.M., Moore, K.J. 1991. Drag reduction in nature. Annual review of fluid mechanics, 23: 65-79.

Castro, A. L., Rosa, R. S. (2005). Use of natural marks on population estimates of the nurse shark, *Ginglymostoma cirratum*, at Atol das Rocas biological reserve, Brazil. Environmental biology of fishes, *72*(2): 213-221.

Chong, M.S., Perry, A.E., Cantwell, B.J. 1990. A general classification of three-dimensional flow fields. Physics of fluids, 2: 765-777. doi:10.1063/1.857730.

Daniel, T.L. 1984. Unsteady aspects of aquatic locomotion. American zoologist, 24(1): 121-134.

Dean, B., Bhushan, B. 2010. Shark-skin surfaces for fluid-drag reduction in turbulent flow: a review. Philosophical transactions of the royal society, 368: 4775-4806.

Drucker, E.G., Lauder, G.V. 1999. Locomotor forces on a swimming fish: three-dimensional vortex wake dynamics quantified using digital particle image velocimetry. Journal of experimental biology, 202: 2393-2412.

Durgin, W.W., Karlsson, S.K.F. 1971. On the phenomenon of vortex street breakdown. Journal of fluid mechanics, 48(3): 507-527.

Eloy,C. 2012. Optimal Strouhal number for swimming animals. Journal of fluids and structures, 30: 205-218.

Epps, B.P., Alvarado, P.V., Youcef-Toumi, K., Techet, A.H. 2009. Swimming performance of a biomimetic compliant fish-like robot. Experimental fluids, 47:927-939.

Esposito, C.J., Tangorra, J.L., Flammang, B.E., Lauder, G.V. 2012. A robotic fish caudal fin: effects of stiffness and motor program on locomotor performance. Journal of Experimental biology, 215: 56-67.

Feldkamp, S.D. 1987. Swimming in the California sea lion: Morphometrics, drag and energetics. Journal of experimental biology, 131: 117-135.

Fish, F.E.1998. Imaginative solutions by marine organisms for drag reduction. International symposium on seawater drag reduction, NUWC, Newport, RI, 443-450.

Fish, F.E. Innes, S., Ronald, K. 1988. Kinematics and estimated thrust production of swimming harp and ringed seals. Journal of experimental biology, 137: 157-173.

Fish, F.E., Shannahan, L.D. 1999. The role of the pectoral fins in body trim of sharks. Journal of fish biology, 56: 1062-1073.

Fish, F.E., Lauder, R.M., Techet, A.H., Triantafyllou, M.S., Walker, J.A., Webb, P.W. 2003. Conceptual design for the construction of a biorobotic AUV based on biological hydrodynamics. Proc. 13th Inter. Symp. Unmanned Untethered Submersible Technology (UUST03), Durham, New Hampshire.

Fish, F.E., Lauder, G.V. 2006. Passive and active control by swimming fishes and mammals. Annual review of fluid mechanics, 38: 193-224.

Fletcher, T., Altringham, J., Peakall, J., Wignall, P., Dorrell, R. 2014. Hydrodynamics of fossil fishes. Royal society, 281: 20140703.

Ferretti, F., Worm, B., Britten, G.L., Heithaus, M.R., Lotze, H.K. 2010. Patterns and ecosystem consequences of shark declines in the ocean. Ecology letters, 13:1055-1071.

Gemballa,S., Konstantinidis, P., Donley, J.M., Sepulveda, C., Shadwick, R.E. 2006. Evolution of high-performance swimming in sharks: transformations of the musculotendinous system from subcarangiform to thunniform swimmers. Journal of morphology, 267:477-493.

Goett, H.J. 1938. Experimental investigation of the momentum method for determining profile drag. National advisory committee for aeronautics, 660:365- 371.

Grace, M.A. 2011. Field guide to requiem sharks (Elasmobranchiomorphi: Carcharhinidae) of the Western North Atlantic. U.S. Dep. Commer. NOAA Technical Report NMFS, 153: 32.

Graham, J.B., Dewar, H., Lai, N.C., Lowell, W.R., Arce, S.M. 1990. Aspects of shark performance determined using a large water tunnel. Journal of experimental biology, 151: 175-192.

Gray, J. 1953. Undulatory propulsion. Nature, 168:551-578.

Gruber, S.H., Nelson, D.R., Morrissey, J.F. 1988. Patterns of activity and space utilization of Lemon Sharks, *Negaprion brevirostris*, in a shallow Bahamian lagoon. Bulletin of marine science, 43(1): 61-76.

Gurka, R. 2003. Coherent structures in turbulent flows. Ph.D. Dissertation, Technion – Israel Institute of Technology. Haifa, Israel.

Gurka, R., Liberzon, A., Hetsroni, G. 2006. POD of vorticity fields: A method for spatial characterization of coherent structures. International journal of heat and fluid flow, 27: 416-423.

Guttridge, T.L., Gruber, S.H., Franks, B.R., Kessel, S.T., Gledhill, K.S., Uphill, J., Krause,J., Sims, D.W. 2012. Deep danger: intra-specific predation risk influences habitat use and aggregation formation of juvenile Lemon sharks *Negaprion brevirostris*. Marine ecology progress series, 445: 279-291.

Hackett, E.E. Luznik, L., Nayak, A.R., Katz, J., Osborn, T.R. 2011. Field measurements of turbulence at an unstable interface between current and wave bottom boundary layers. Journal of geophysical research, 116, C02022.

Harris, J. E. 1936. The role of the fins in the equilibrium of the swimming fish. I. Wind-tunnel tests on a model of *Mustelus canis* (Mitchill). Journal of experimental biology, 13: 476–493.

Heckmati, A. Ricot, D., Druault, P. 2011. About the convergence of POD and EPOD modes computed from CFD simulation. Computers & fluids, 50(1): 60-71.Gr

Hertel, H. 1966. Structure, form and movement. Reinhold, New York, NY.

Imron,C., Widodo, B., Yuwono, T.Y. 2017. The effectiveness of passive control to reduce the drag coefficient. Journal of physics: Conference series, 890: 012044.

Irschick, D.J., Fu, A., Lauder, G., Wilga, C., Kuo, C., Hammerschlag, N. 2017. A comparative morphological anlysis of body and fin shape for eight shark species. Biological journal of the linnean society, 122(3): 589-604.

Kempf, G., Neu, W., 1932. Schleppversuche mit Hechten zur Messung des Wasserwiderstandes. Jounral of computational physics, 17: 353-364.

Kim, S., Huang, W., Sung, H.J. 2010. Constructive and destructive interaction modes between two tandem flexible flags in viscous flow. Journal of fluid mechanics, 661: 511-521.

Kolmogorov, A.N. 1941. The local structure of turbulence in incompressible viscous fluid for very large Reynolds numbers. C.R. Academy of Science URSS, 30:301.

Kozlov, A., Chowdhury, H., Mustary, I., Loganathan, B., Alam, F.2015. Bio-inspired design: aerodynamics of boxfish. Procedia engineering, 105: 323-328.

Kulkarni, A.A., Patel, R.K., Friedman, C., Leftwich, M.C. 2017. A robotic platform to study the foreflipper of the California Sea Lion. Journal of visual experiments (119), e54909.

Langton, S.G. 2007. Euler on rigid bodies. Leonhard Euler: Life, work, and legacy, 5(1): 195-211.

Lauder,G.V., Tytell, E.D. 2006. Hydrodynamics of undulatory propulsion. Fish Biomechanics, 23:425-468.

Lingham-Soliar, T. 2005. Dorsal fin in the white shark, *Carcharodon carcharias*: A dynamic stabilizer for fast swimming. Journal of morphology, 263:1-11.

Lighthill, M.J. 1970. Aquatic animal propulsion of high hydromechanical efficiency. Journal of fluid mechanics, 44(2):265-301.

Lindsey, C. C. 1978. Form, function, and locomotory habits in fish. Fish physiology, 7:1–100. Academic Press, New York.

Liu, G., Ren, Y., Dong, H., Akanyeti, O., Liao, J.C., Lauder, G.V. 2017. Computational analysis of vortex dynamics and performance enhancement due to body-fin and fin-fin interactions in fish-like locomotion. Journal of fluid mechanics, 829: 65-88.

Liu, S., Meneveau, C., Katz, J. 1994. On the properties of similarity subgrid-scale models as deduced from measurements in a turbulent jet. Journal of fluid mechanics, 275: 83-119.

Lumley, J. 1970. Stochastic tools in turbulence. Dover publications.

Maia, A., Lauder, G.V., Wilga, C.D. 2017. Hydrodynamic function of dorsal fins in spiny dogfish and bamboo sharks during steady swimming. Journal of experimental biology, 220: 3967-3975.

Maertens, A.P., Triantafyllou, M.S., Yue, D.K.P. 2015. Efficiency of fish propulsion. Bioinspiration and biomimetics, 10: 1-11.

Marius, S.D., Anca, S.C. 2012. Fluid-structure interaction. Fluid dynamics, computational modeling and applications Dr. L. Hector Juarez (Ed.). ISBN: 978-953-51-0052-2, InTech, 194-216.

Melling, A. 1997. Tracer particles and seeding for particle image velocimetry. Measurement science and technology, 8: 1406–1416.

Moss, S.A. 1984. Sharks: an introduction for the amateur naturalist. Prentice-Hall, Inc., Englewood Cliffs, New Jersey. 246.

Naudascher, E. 1965. Flow in the wake of self-propelled bodies and related sources of turbulence. Journal of fluid mechanics, 22(4): 625-656.

Nesteruk, I, Passoni, G, Redaelli, A. 2014. Shape of aquatic animals and their swimming efficiency. Journal of marine biology, 1-9 470715.

Nogueria, J., Lecuona, A., Rodriguez, P.A. 1997. Data validation, false vectors correction and derived magnitudes calculation on PIV data. Measurement science and technology, 8: 1493-1501.

Payne, N.L., Iosilevskii, G., Barnett, A., Fischer, C., Graham, R.T., Gleiss, A.C., Watanabe, Y.Y. 2016. Great hammerhead sharks swim on their side to reduce transport costs. Nature communications, 1-5.

Pnueli, D., Gutfinger, C. 2000. Fluid mechanics. Cambridge, United Kingdom. Cambridge University Press.

Pope, S. 2000. Turbulent flows. Cambridge University Press. New York, NY.

Price, J.F. 2006. Langrangian and Eulerian representations of fluid flow: Kinematics and the equations of motion. Woods hole oceanographic instiution, Woods Hole, MA.

Raffel, M., Willert, C.E. and Kompenhans, J. 1998. Particle image velocimetry: a practical guide. Springer science & business media.

Rossi, C., Colorado, J., Coral, W., Barrientos, A. 2011. Bending continuous structures with SMAs: a novel robotic fish design. Bioinspiration and biomimetics, 6(4): 1-15.

Saddoughi, S. and Veeravalli, S. 1994. Local isotropy in turbulent boundary layers at high Reynolds number. Journal of fluid mechanics, 268: 333-372.

Sagong, W., Jeon,W-P., Choi, H. 2013. Hydrodynamic characteristics of the Sailfish (*Istiophorus platpterus*) and Swordfish (*Xiphias gladius*) in gliding postures at their cruise speeds. PLoS one, 8(12):e81323.

Shadwick, E.R., Gemballa, S., 2006. Structure, kinematics, and muscle dynamics in undulatory swimming. Fish biomechanics, 241-280.

Sirovich, L. 1987. Turbulence and the dynamics of coherent structures part I: coherent structures. Quarterly of applied mathematics, 45(3): 561-571.

Smith, M.F.L., Marshall, A., Correia, J.P., Rupp, J. 2004. Elasmobranch transport techniques and equipment. The elasmobranch husbandry manual: Captive care of sharks, rays and their relatives, 105-131.

Stalnov, O., Ben-Gida, H., Kirchhefer, A.J., Guglielmo, C.G., Kopp, G.A., Liberzon, A., Gurka, R.2015. On the estimation of time dependent lift of a European starling (*Sturnus vulgaris*) during flapping flight. PLoS ONE, 10(9): e0134582.

Stanek, M.J. 2018. Characterization of a turbulent boundary layer in open channel flow using particle image velocimetry. Electronic thesis and dissertations 48, Coastal Carolina University. Conway, South Carolina.

Sundnes, G. 1963. Energy metabolism and migration of fish. ICNAF Environmental symposium, 6: 743-746.

Sundström , L.F., Gruber,S.H., Clermont, S.M., Correia , J.P.S., de Marignac, J.R.C., Morrissey, J.F., Lowrance, C.R., Thomassen ,L. & Oliveira, M.T. 2001. Review of elasmobranch behavioral studies using ultrasonic telemetry with special reference to the Lemon shark, *Negaprion brevirostris*, around Bimini Island, Bahamas. Environmental biology of fishes, 60 (1-3): 225-250.

Taylor, G.K., Nudds, R.L., Thomas, A.L.R. 2003. Flying and swimming animals cruise at a Strouhal number tuned for high power efficiency. Nature, 707-711.

Taylor, Z.J. 2011. The mechanisms of vortex shedding from elongated bluff bodies. Ph.D. Dissertaion, The University of Western Ontario. Ontario, Canada.

Taylor, Z.J., Liberzon, A., Gurka, R., Holzman, R., Reesbeck, T., Diez, F.J. 2013. Experiments on the vortex wake of a swimming knifefish. Experimental fluids, 54(8):54-57.

Thomson, K.S. 1976. On the heterocercal tail in sharks. Paleobiology, 2:19-38.

Thomson, K.D., Morrison, D.F. 1971. The spacing, position and strength of vortices in the wake of slender cylindrical bodies at large incidence. Journal of fluid mechanics, 50(4): 751-783.

Thomson, K.S., Simanek, D.E. 1977. Body form and locomotion in sharks. American zoologist, 17: 343-354.

Tytell, E.D. 2006. Median fin function in bluegill sunfish *Leopomis macrochirus*: streamwise vortex structure during steady swimming. Journal of experimental biology, 209:1516-1534.

Videler, J.J. 1993. Fish swimming. London, UK: Chapman & Hall.

Von Kármán, T., Millikan, C.B. 1934. On the theory of laminar boundary layers involving separation. NACA Report 504.

Von Kármán, T.1937. The fundamentals of the statistical theory of turbulence. Journal of the aeronautical sciences, 4(4): 131-138.

Von Kármán, T. and Sears, W.R. 1938. Airfoil Theory for Non-Uniform Motion. Journal of the aeronautical sciences, 5(10): 379-390.

Ward-Paige, C.A., Britten, G.L., Bethea, D.M., Carlson, J.K. 2015. Characterizing and predicting essential habitat features for juvenile coastal sharks. Marine ecology, 36: 419-431.

Webb, P.W. 1971. The swimming energetics of trout I. thrust and power output at cruising speeds. Journal of experimental biology, 55: 489-520.

Webb, P. W. 1975. Hydrodynamics and energetics of fish propulsion. Fishery bulletin, 190: 1–159.

Webb, P. W. 1978. Hydrodynamics: Nonscombroid fish. Fish physiology, 7:189–237. Academic Press, New York.

Webb, P.W., Keyes, R.S. 1982. Swimming kinematics of sharks. Fishery bulletin, 4(80): 803-812.

Webb, P.W., Kostecki, P.T. 1984. The effect of size and swimming speed on locomoter kinematics of rainbow trout. Journal of experimental biology, 109:77-95.

Webb, P. W., Weihs, D. 1983. Fish biomechanics. Praeger Publishers, New York.

Westerweel J, Dabiri D, Gharib M. 1997 The effect of a discrete window offset on the accuracy of cross-correlation analysis of digital PIV recordings. Experiments in fluids, 23(1):20-8.

Wetherbee, B., Gruber, S., Cortes, E. 1990. Diet, feeding habits and consumption in sharks, with special reference to the Lemon shark, *Negaprion brevirostris*. Elasmobranchs as living resources, 29-47.

Wilga, C.D., Lauder, G.V.2000. Three-dimensional kinematics and wake structure of the pectoral fins during locomotion in the leopard sharks *Triakis semifasciata*. Journal of experimental biology, 203: 2261-2278.

Wilga, C.D., Lauder, G.V. 2002. Function of the heterocercal tail in sharks: quantitative wake dynamics during steady horizontal swimming and vertical maneuvering. Journal of experimental biology, 205: 2365-2374.

Willert,C.E., Gharib, M. 1991. Digital particle image velocimetry. Experiments in fluids, 10:181-193.

Williams,T.M., Kooyman, G.L. 1985. Swimming performance and hydrodynamic characteristics of Harbor seals *Phoca vitulina*. Physiological and biochemical zoology, 58(5): 576-589.

Wolfgang, M.J., Anderson, J.M., Grosenbaugh, M.A., Yue, D.K.P., Triantafyllou, M.S. 1999. Near-body flow dynamics in swimming fish. Journal of experimental biology, 202: 2303-2327.

Wu, T.Y., 1971. Hydromechanics of swimming propulsion. Part 3. Swimming and optimum movements of slender fish with side fins. Journal of fluid mechanics 46(3): 545-568.